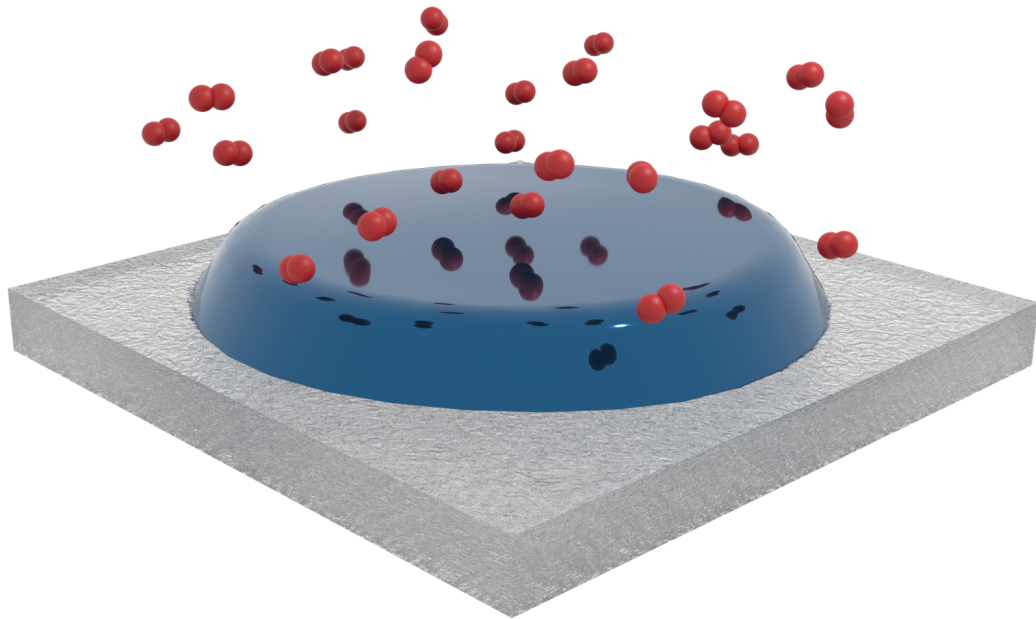




**CHALMERS**  
UNIVERSITY OF TECHNOLOGY

---



# **Optical response of nanoalloy hydrogen sensors from first-principles**

Master's thesis in Applied Physics

VICTOR ROSENDAL



MASTER'S THESIS 2020

# Optical response of nanoalloy hydrogen sensors from first-principles

Victor Rosendal



**CHALMERS**  
UNIVERSITY OF TECHNOLOGY

Department of Physics  
*Division of Condensed Matter and Materials Theory*  
CHALMERS UNIVERSITY OF TECHNOLOGY  
Gothenburg, Sweden 2020

Optical response of nanoalloy hydrogen sensors from first-principles  
Victor Rosendal

© Victor Rosendal, 2020.

Supervisor: Paul Erhart, Department of Physics  
Examiner: Paul Erhart, Department of Physics

Master's Thesis 2020  
Department of Physics  
Division of Condensed Matter and Materials Theory  
Chalmers University of Technology  
SE-412 96 Gothenburg  
Telephone +46 31 772 1000

Cover: Illustration of the hydrogen sensor. The red spheres represents hydrogen and the blue metallic disk is the sensor. The disk is on top of a silica substrate.

Typeset in L<sup>A</sup>T<sub>E</sub>X  
Printed by Chalmers Reproservice  
Gothenburg, Sweden 2020

Optical response of nanoalloy hydrogen sensors from first-principles  
Victor Rosendal  
Department of Physics  
Chalmers University of Technology

## Abstract

Hydrogen shows promise as a replacement for conventional fossil fuels. However, its high flammability and gas permeability pose high demands on sensors, which must respond quickly and accurately. Nanoscaling improves the kinetics and allows for optical hydrogen sensing. A nanoscaled metallic sensor typically shows a well-defined extinction peak in the optical regime and one proposed sensing technique is to detect the shift in said peak due to hydrogenation.

The aim of this thesis is to, from first-principles, study the optical response of PdAu nanodisks as a function of hydrogenation. PdAu:H was mainly treated as a random alloy but thermodynamic structures were also investigated. Cluster expansions were used in combination with Monte Carlo simulations to generate thermodynamically representative PdAu:H structures. The dielectric functions for the random and the thermodynamic structures were calculated by applying static and time-dependent density functional theory. Optical extinction spectra of PdAu:H nanodisks were obtained via electromagnetic finite-difference time-domain simulations using the previously calculated dielectric functions.

The extinction peak of nanodisks with a diameter of 100 nm and height 20 nm showed a redshift due to hydrogenation over the entire range of gold concentrations of 0 to 42% considered here, and the redshift is approximately linear with respect to hydrogen. Even though there is non-trivial ordering in the thermodynamic PdAu:H structures, no clear difference between the random and thermodynamic case was observed in the optical response.

Keywords: hydrogen, sensing, palladium, gold, nanodisk, extinction, spectra, plasmonics, TDDFT, DFT.



## Acknowledgements

I would like to thank my supervisor and examiner Paul Erhart for all of the guidance and support throughout the project. I would furthermore like to thank Magnus Rahm for his assistance and help with everything between technical issues to physical interpretations. I also want to thank Tuomas Rossi for sharing his knowledge, especially regarding the FDTD electromagnetic simulations. Without the three of you the project would not have been the same.

Finally, I want to thank my family and friends for the support through out my studies.

Victor Rosendal, Gothenburg, July 2020



# Contents

<b>List of Figures</b>	<b>xi</b>
<b>List of Tables</b>	<b>xiii</b>
<b>Glossary</b>	<b>xv</b>
<b>1 Introduction</b>	<b>1</b>
<b>2 Atomic structure of PdAu:H</b>	<b>5</b>
2.1 Theory of cluster expansions . . . . .	5
2.2 Special structures . . . . .	7
2.3 Short-range order in PdAu:H . . . . .	7
2.4 Summary . . . . .	8
<b>3 Electronic properties of PdAu:H</b>	<b>11</b>
3.1 Introduction to density functional theory . . . . .	11
3.1.1 Hohenberg-Kohn theorems . . . . .	12
3.1.2 Kohn-Sham ansatz . . . . .	13
3.2 Ground state density functional theory results . . . . .	13
3.2.1 Lattice expansion of the PdAu:H alloy . . . . .	14
3.2.2 Band structure of PdAu:H . . . . .	15
3.2.3 Electronic density of states of the alloy . . . . .	17
3.3 Summary . . . . .	18
<b>4 Dielectric response of PdAu:H</b>	<b>19</b>
4.1 Introduction to time-dependent DFT . . . . .	19
4.1.1 Linear response and dielectric function . . . . .	19
4.2 Convergence of TDDFT parameters . . . . .	21
4.3 Dielectric response of PdAu:H . . . . .	23
4.4 Summary . . . . .	27
<b>5 Lorentzian representation of dielectric functions</b>	<b>29</b>
5.1 Fitting method . . . . .	30
5.2 Examples of Lorentzian fits . . . . .	33
5.3 Summary . . . . .	34
<b>6 Optical response of PdAu:H nanodisks</b>	<b>35</b>

6.1	Finite-difference time-domain method . . . . .	35
6.2	Convergence and performance of MEEP . . . . .	37
6.3	Absorption or scattering . . . . .	41
6.4	Response due to lattice expansion . . . . .	42
6.5	Total response due to hydrogenation . . . . .	42
6.6	Response of disks with different aspect ratios . . . . .	45
6.7	Impact of microscopical configuration . . . . .	47
6.8	Summary . . . . .	49
<b>7</b>	<b>Discussion and conclusion</b>	<b>51</b>
7.1	Ordering of PdAu:H alloy and its effect on spectra . . . . .	51
7.2	Electronic structure and dielectric response for PdAu:H . . . . .	52
7.3	Optical response due to hydrogenation . . . . .	52
	<b>Bibliography</b>	<b>53</b>

# List of Figures

1.1	PdAu face-centred cubic lattice with H interstitial lattice . . . . .	2
2.1	Usage of cluster expansions in this thesis . . . . .	5
2.2	Short range order of the PdAu:H alloy . . . . .	8
3.1	Hohenberg-Kohn theorems and Kohn-Sham ansatz . . . . .	11
3.2	Lattice parameters of PdAu:H special quasi-random structures . . .	14
3.3	Unfolded band structures for PdAu:H special quasi-random structures	15
3.4	Density of states for special quasi-random structures of PdAu . . . .	16
3.5	Density of states for special quasi-random structures of PdAu:H . . .	16
3.6	Shift of d-band edge with Au and H content . . . . .	17
4.1	Convergence of dielectric function with computational parameters . .	22
4.2	Dielectric functions for Pd <sub>0.75</sub> Au <sub>0.25</sub> :H alloys as a function of H content	23
4.3	Loss functions of PdAu:H special quasi-random structures . . . . .	24
4.4	Comparison between loss functions of PdAu:H special ordered structures and special quasi-random structures . . . . .	25
4.5	Visible regime of the loss functions for PdAu:H special quasi-random structures . . . . .	25
4.6	Constant-energy slices of the real part of the dielectric function for Pd:H . . . . .	26
5.1	Overview of Lorentzian fitting method . . . . .	29
5.2	Proof of concept of the fitting methods in combination with information criteria . . . . .	32
5.3	Optical spectra of a gold sphere with different number of Lorentzians	32
5.4	Typical Lorentzian representation of dielectric function . . . . .	33
5.5	Illustration of overfitting and the difference between two experimentally obtained dielectric functions . . . . .	34
6.1	Sketch of the finite-difference time-domain computational cell . . . .	37
6.2	Convergence of the calculated optical spectra . . . . .	38
6.3	Illustration of the impact of resolution on the optical response . . . .	39
6.4	Computational cost of the MEEP simulations . . . . .	40
6.5	Strong scaling of the MEEP simulations . . . . .	40
6.6	Variation of optical spectra with cone geometry . . . . .	41
6.7	Impact of lattice expansion due to hydrogen on the optical spectra . .	42

6.8	Spectra for the truncated cone geometry with diameter 100 nm and height 20 nm . . . . .	43
6.9	Heat map of the absorption efficiency for different hydrogen concentrations . . . . .	44
6.10	Heat map of peak absorption energy as a function of gold and hydrogen concentration . . . . .	45
6.11	Absorption peak position as a function of hydrogen content . . . . .	45
6.12	Absorption peak position for different aspect ratios . . . . .	46
6.13	Calculated sensitivities from FDTD simulations compared to experimental data . . . . .	47
6.14	Optical spectra of special quasi-random structure and special ordered structure versions of $\text{Pd}_{0.83}\text{Au}_{0.17}$ and $\text{Pd}_{0.83}\text{Au}_{0.17}\text{H}_{0.67}$ . . . . .	48
6.15	Red-shift of the absorption peak for ordered and random structures .	48

# List of Tables

4.1	Converged parameters for ground state and time-dependent density functional theory calculations. . . . .	23
6.1	Parameters for MEEP production runs. . . . .	40



# Glossary

- AIC** Akaike information criterion. 31, 32
- AR** aspect ratio. 41, 45–47, 49, 52
- BIC** Bayesian information criterion. 31, 32, 34
- CE** cluster expansion. 5–7, 51
- DF** dielectric function. 19, 21–23, 26, 27, 29–31, 33–35, 37, 39, 40, 45, 49, 51, 52
- DFT** density functional theory. 5–7, 11, 13, 15, 18, 19, 21, 23, 51
- DOS** density of states. 14, 16–18, 52
- FCC** face-centred cubic. 1, 2, 7, 14
- FDTD** finite-difference time-domain. 32, 35–37, 42, 45, 47
- FWHM** full width at half maximum. 37, 38
- KS** Kohn-Sham. 13, 19–21
- LASSO** least absolute shrinkage and selection operator. 29–32
- LSPR** localised surface plasmon resonance. 2
- MC** Monte Carlo. 5–8, 51
- OMP** orthogonal matching pursuit. 29–32
- PML** perfectly matched layer. 36–38, 40
- RPA** random phase approximation. 20, 21
- SOS** special ordered structure. 7, 9, 14, 18, 24, 25, 27, 47–49, 51
- SQS** special quasi-random structure. 7, 9, 14–18, 23–25, 27, 47–49, 51
- SRO** short-range order. 7–9
- TDDFT** time-dependent density functional theory. 19, 21, 22, 27, 29, 30, 34, 35, 51



# 1

## Introduction

A hydrogen economy could play an important role in achieving a low carbon society. The idea behind a hydrogen economy is to use hydrogen gas as an energy carrier instead of gasoline, diesel or any other fossil fuel. Hydrogen gas is advantageous compared to the latter, since a reaction between gas and oxygen only produces water. In other words, hydrogen gas has the possibility of being an energy carrier with zero green house gas emission.

The hydrogen economy does, however, come with some flaws and drawbacks. Most of these problems stem from the intrinsic properties of the gas itself, mainly the fact that hydrogen is a colourless, odourless, highly permeable *and* highly flammable gas. A combination of these properties is unwanted since the high permeability of the gas leads to a high risk of leakage. Once the flammable gas is leaked it is difficult to detect. To be able to safely use hydrogen as fuel in any application there is therefore a vital need for sensors that are reliable, fast, and accurate. This need for viable hydrogen sensors can be seen in the growing number of publications related to hydrogen sensors that are published every year. While there are several possible sensing techniques, electrical and optical sensors are the most common [1]. An electrical hydrogen sensor typically measures the resistivity of a metal as a function of the absorbed hydrogen content. This change in resistivity originates from the fact that the electrons scatter with the absorbed hydrogen and therefore the resistivity is increased with an increase in hydrogen content. In the case of an optical sensor, the hydrogen content affects the optical properties such as absorption and scattering spectra of the metal (in other words its colour). The main advantage of optical sensors over electrical ones is the that the readout can be done remotely and that there is no risk of creating sparks that can be caused by an electrical current.

To fulfil the requirements of a fast and responsive hydrogen sensor, one often uses palladium as the active part of the sensor. Palladium has a strong affinity to hydrogen and causes the surrounding hydrogen molecules to dissociate, with little to no activation barrier. The hydrogen atoms are absorbed and diffuse into the palladium lattice [2]. The individual hydrogen atoms then reside at octahedral interstitial sites of the palladium face-centred cubic (FCC) lattice, see Figure 1.1.

While pure palladium is a good catalyst, like many other single metal systems it has a major disadvantage when it comes to hydrogen sensing: When one increases the surrounding hydrogen pressure the hydrogen content in the metal slowly increases until a critical point is reached. Further increasing the hydrogen pressure rapidly increases the hydrogen concentration. This phenomena is known as the plateau and occurs at the hydride formation pressure [3]. As a result the output from the single metallic sensor is nonlinear and therefore not ideal. Above the so called critical

temperature the plateau vanishes, making it possible to get a continuous readout from the sensor.

It has been demonstrated that alloying palladium with other metals can reduce the critical temperature to below room temperature, thereby removing the plateau of the sensor in working conditions [4]. This behaviour has been used by researchers to create plateau free optical hydrogen sensors based on palladium alloys. Zhao *et al.* showed that by using a thin film of palladium-gold alloy the response time of the hydrogen sensor was further improved [5].

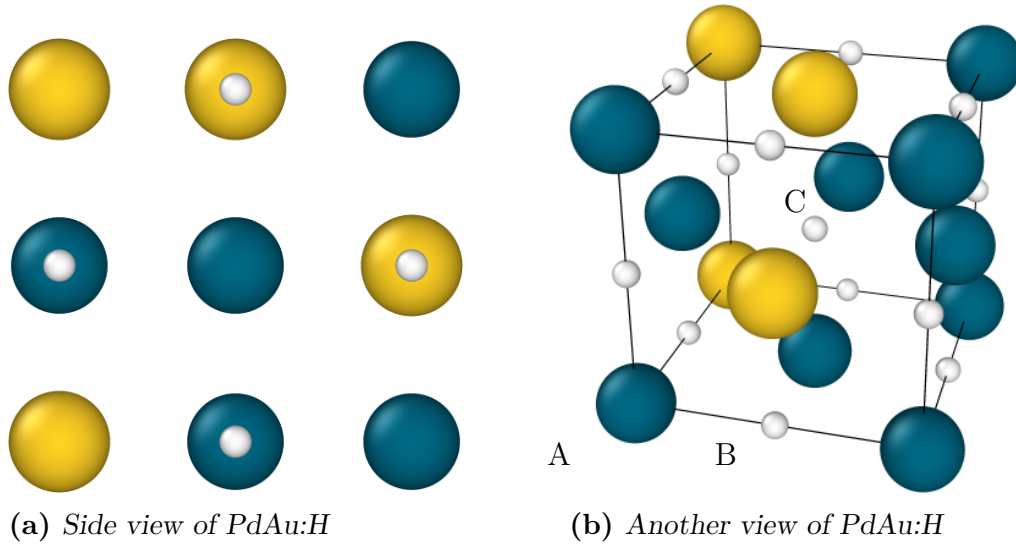


**Figure 1.1:** Illustration of the PdAu FCC lattice with hydrogen in octahedral interstitial positions. Hydrogen is represented by a small white sphere, while palladium and gold are blue and golden coloured, respectively. There is one interstitial lattice point per metal atom. Removing a hydrogen atom creates a vacancy. The palladium at A and hydrogen at B form a nearest neighbour pair between two so called sublattices. A second nearest neighbour between the two sublattices would be between palladium at A and hydrogen at C.

There has been a great interest in nanosizing optical sensors recently due to the special properties that emerge when the particle size is comparable to or smaller than the wavelength of the light. These metallic nanosized particles have sharp absorption and scattering peaks due to localised surface plasmon resonances (LSPRs). LSPR is not only sensitive to the dielectric properties of the material and the environment but it is also highly sensitive to particle geometry and size [6]. Sensors based on LSPR typically measure a difference in resonance peak position, width or height due to a change in the environment or in the particle itself. It is therefore possible to alter the shape and size of a nanoparticle with a given active sensing material to tailor the optical spectrum. In other words, LSPR sensors have additional tunable properties compared to surface or bulk sensors. These types of optical sensors are advantageous in hydrogen sensing since the particles are on the nanoscale and therefore the diffusion time is reduced. Low diffusion times are essential since they reduce the possibility that the response time is limited by diffusion. Previous research has shown that LSPR-based hydrogen sensors of nanoparticles made of palladium-gold

alloy are viable and meet targets of the automotive industry [7].

This thesis aims at calculating the optical response of palladium-gold hydrogen sensors from first principles. This will be done for a range of palladium-gold concentrations and for different shapes and sizes of the sensor. Experimental measurements of optical hydrogen sensors typically result in an optical spectrum containing the plasmonic peak that is used for sensing. The measured optical spectrum is a convolution of the dielectric properties and the shape of the system. First principles calculations are therefore extremely valuable since one can disconnect the underlying material properties from the shape of the particle that results in the observable spectrum. Another advantage these simulations are that it is possible to control all parameters and thereby sample the whole parameter space.

The thesis is structured in the following way: first chapter describes how representative structures of palladium-gold-hydride can be constructed, here both random structures and thermodynamically representative structures will be treated. In the following chapter the ground state electronic properties of these structures will be presented and discussed. The dielectric response of said systems will then be investigated in subsequent chapter. In the end the optical response will be calculated and studied for different sizes and shapes of nanosensors. This is done by using an electromagnetic simulation software. This software expect the materials to be described on a specific form, the transformation from raw data to this form will be treated in chapter 5.



# 2

## Atomic structure of PdAu:H

This chapter introduces the cluster expansion (CE) technique and presents the results from CE-based Monte Carlo (MC) simulations of PdAu:H. This is needed to obtain thermodynamically representative structures. Random structures will also be generated. Random and thermodynamic structures will also be converted into smaller special structures that incorporate the ordering of the larger cells. CE were constructed and MC simulations were carried out using the `icet` and `mchammer` packages [8]. In Figure 2.1 the power of CEs is illustrated. By training the CEs on known target configurations one can predict quantities of any other configuration. This prediction is computationally highly efficient, which enables sampling by MC simulations.

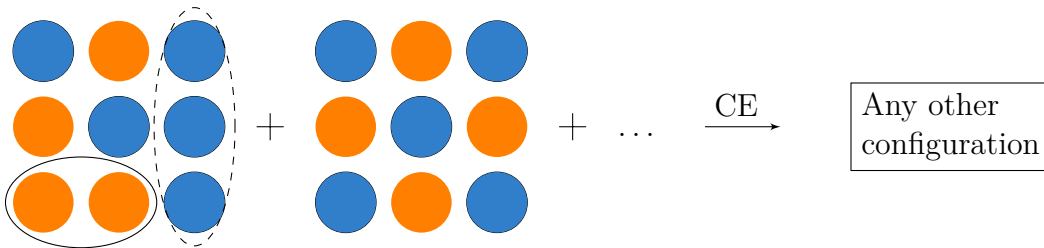


**Figure 2.1:** Usage of CEs in this thesis. Structures are decomposed into clusters, i.e. pairs, triplets and so on. By having access to the value of a quantity (in this case energies from density functional theory (DFT)) for many structures a CEs can be constructed and used to predict the energy of any configuration. This is done by finding the energy contribution for every type of cluster and then these values can be used to predict the energy of a new, arbitrary, configuration. This is possible since any other configuration can be seen as a combination of clusters.

### 2.1 Theory of cluster expansions

A CE is a function that maps the microscopic configuration of a structure to a property. It is a powerful tool that allows one to evaluate the quantity, typically an energy, of a system by viewing the system as a set of clusters or bonds that contribute to the total value of the quantity. In this section, the quantity is an energy and it is assumed that the system is an alloy where each lattice point can be occupied by either atom A or B. Strictly speaking the PdAu:H alloy studied contains two sublattices, one for palladium/gold and one for hydrogen/vacancy, see Figure 1.1. Nevertheless, the fundamentals are the same.

The simplest kind of CEs is an expansion that only takes nearest neighbour pairs into account. By assigning values to the atoms  $\sigma_A = +1$  and  $\sigma_B = -1$ , one can evaluate the product of these values for all pairs in the cell (while avoiding double counting the pairs). If it is known how much each A-A (and B-B) and A-B pairs contribute one can evaluate the total energy as:

$$E = J_0 + J_1 \sum_i \sigma_i + J_2 \sum_{\langle ij \rangle} \sigma_i \sigma_j,$$

where  $J_0$  is a constant offset,  $J_1$  can be seen as the contribution from the different atoms to the total energy and  $J_2$  is the energy due to the different types of pairs. This is the famous Ising model. Here  $\langle ij \rangle$  denotes that  $i$  and  $j$  should be nearest neighbours. All of the chemistry is hidden in the unknown parameters  $J_n$  and this is the strength (and possible weakness) of CEs. For the expansion to be predictive, the parameters must be known and of good accuracy. Clearly if there is a significant long-range interaction, this simple nearest-neighbour model will not be very useful. The Ising model above is a limited case of the general CE. Without any more detailed theory the CE is defined as [8]:

$$E(\boldsymbol{\sigma}) = E_0 + \sum_{\alpha} \langle \Pi_{\alpha'} \rangle_{\alpha} m_{\alpha} J_{\alpha} = \boldsymbol{\omega}(\boldsymbol{\sigma}) \cdot \mathbf{J}, \quad (2.1)$$

where  $\boldsymbol{\sigma}$  is a vector over all lattice points with elements  $+1$  or  $-1$  (in the simple binary case) depending on what element is occupying the lattice point. The sum is over all symmetry inequivalent clusters  $\alpha$  (e.g., singlet, pairs, triplets etc.) and  $\langle \dots \rangle_{\alpha}$  denotes averaging over all clusters,  $\alpha'$ , symmetrically equivalent to  $\alpha$ . The multiplicity of the cluster  $\alpha$  is denoted  $m_{\alpha}$ . In the binary case,  $\Pi_{\alpha'}$  is the product  $\sigma_0 \sigma_1 \dots \sigma_{N-1}$ , where  $N$  is the number of points in the cluster, i.e., 1 for a singlet, 2 for pairs and so on. It should be noted that this infinite expansion, that in principle is exact, must be truncated for practical applications. This truncation can be motivated by the fact that very long-range interactions should be negligible.

The energy  $E(\boldsymbol{\sigma})$  can be evaluated, typically using DFT, for a set of configurations. The unknown interaction vector  $\mathbf{J}$  can then be evaluated by solving the matrix equation:

$$\mathbf{E} = \mathbf{\Pi} \mathbf{J},$$

where  $\mathbf{E}$  contains the target energy for each configuration and each row in the matrix  $\mathbf{\Pi}$  contains the so-called cluster vector,  $\mathbf{\Pi}_i = \boldsymbol{\omega}(\boldsymbol{\sigma})$ , for each structure. If the parameters  $\mathbf{J}$  are known the entire expansion is determined and the energy for any configuration can be evaluated.

Since the energy is expressed as a function of only the occupation, this method is extremely efficient, which makes MC simulations feasible using DFT data as input. Without a CE each MC step would require a new DFT calculation, but this method allows one to quickly approximate the energy within tolerable errors for any sampled configuration. MC simulations are useful if it is of interest to study the thermodynamically representative structures, compared to totally random structures, see the following section.

## 2.2 Special structures

Combining CEs and MC simulations makes it possible to iterate through different, energetically favourable, configurations of the alloy. By averaging the cluster vector,  $\omega(\sigma)$ , over many iterations the cluster vector will converge to some thermodynamic average. This cluster vector encodes the structural correlation present in the system. In this thesis random alloys will also be investigated. The naive approach is to randomly occupy each lattice point with either palladium or gold (and hydrogen or vacancy) up to some defined concentration. This is, however, not efficient since it would require very large unit cells, for which DFT are computationally extremely expensive. It is however possible to create a cluster vector that represents a random alloy.

By defining a so-called cluster space it is then possible to convert the cluster vector, either from MC simulation or randomized structures, to a smaller unit cell [9, 10]. The cluster space is a set of all the available clusters. One typically limits the cluster space by setting a cutoff on the distances between points in pairs and triplets and so on. The cutoffs were set to  $1.35a$  and  $1.05a$  for pairs and triplets, respectively, where  $a$  is the lattice parameter. In the random case, the resulting smaller cell is a so-called special quasi-random structure (SQS) and it approximates the correlation of a completely random alloy. Similarly a smaller unit cell can be generated from the MC cluster vector that approximately incorporates the correlations from said cluster vector, in this thesis such constructions will be referred to as special ordered structures (SOSs).

## 2.3 Short-range order in PdAu:H

To generate thermodynamically representative structures (that subsequently were turned into SOSs), MC simulations were carried out. The energy was evaluated using a CE<sup>1</sup>, as described above.

For every gold concentration a random palladium-gold FCC lattice was constructed. Then each of these structures was (partially) filled with hydrogen at the interstitial points of the FCC lattice, see Figure 1.1. Then a canonical ensemble MC simulation at 300 K was carried out using the PdAu:H CE where only the hydrogen atoms are allowed to change position in the lattice. In other words it is assumed that the palladium-gold lattice is frozen at 300 K. The canonical MC simulation was run for  $N_{\text{atoms}} = 1728$  steps repeated  $N_{\text{runs}} = 50$  times. Here,  $N_{\text{atoms}}$  is the number of sites in the supercell. Each  $N_{\text{atoms}}$  steps the current cluster vector of the structure was added to a total cluster vector and in the end this sum was divided by  $N_{\text{runs}}$ . In other words by doing this, one obtains an average representation of the structure described by the resulting average cluster vector. This average cluster vector was then transformed into a SOS of 12 metal atoms, as described in section 2.2.

The short-range order (SRO) parameter,  $\alpha$ , describes how probable it is to find Pd-H and Au-V pairs relative to all other possible pairs. The SRO parameter evaluates

<sup>1</sup>In this thesis an already existing CE was used.

this probability relative to the concentrations, as seen below [11].

$$\alpha = 1 - \frac{\text{Pd-H} + \text{Au-V}}{\text{Pd-H} + \text{Au-V} + \text{Pd-V} + \text{Au-H}} \frac{1}{c_{\text{H}}c_{\text{Pd}} + c_{\text{V}}c_{\text{Au}}}.$$

Here,  $c_i$  is the concentration of species  $i$  and a vacancy is denoted V. Note that the Pd-Au and H-V lattices are separate sublattices that fulfil  $1 = c_{\text{Pd}} + c_{\text{Au}}$  and  $1 = c_{\text{H}} + c_{\text{V}}$ , respectively. The SRO parameter for the average structure generated by MC simulations is presented in Figure 2.2, which shows both the nearest neighbour (NN) and second nearest neighbour (2nd NN) version of the SRO parameter. The formula is equivalent, but the difference lies in which cluster (bond) is being counted. From the figure it can be seen that there is some ordering since the SRO parameter is non-zero for the cases with gold. Furthermore, in the NN regime the SRO parameter is negative which indicates that palladium-hydrogen (as well as gold-vacancy) pairs are preferable. By contrast, in the 2nd NN regime palladium-vacancy (and gold-hydrogen) pairs are favourable.

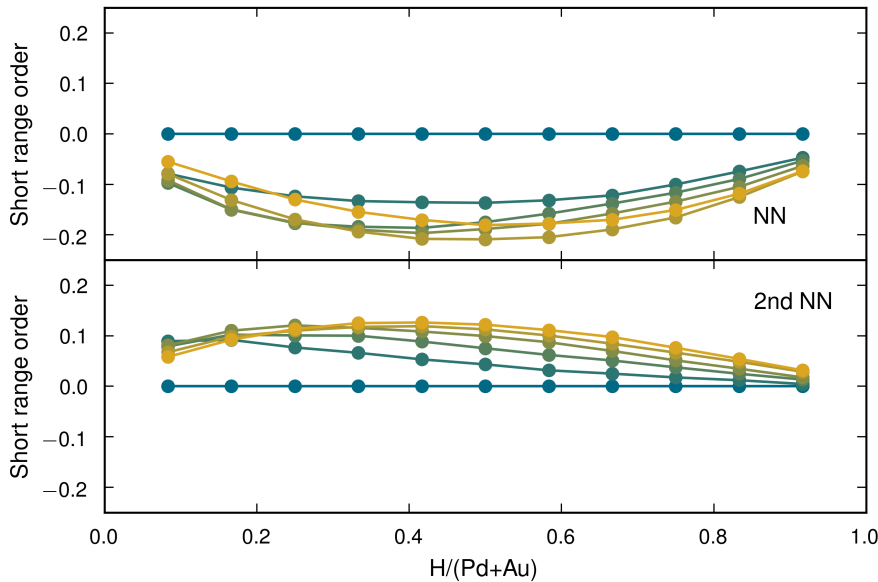


**Figure 2.2:** Short range order of the PdAu:H alloy. The most blue line correspond to Pd:H and higher gold concentration is represented by a more golden colour. In the upper figure the nearest neighbour SRO parameter is shown and in the lower figure the second nearest neighbour SRO parameter is presented. The negative sign of the NN SRO indicates that Pd-H and Au-V pairs are more common than Pd-V and Au-H, at very short distances. Looking at second NN it is clear, by the positive sign, that Pd-V and Au-H pairs are more probable.

## 2.4 Summary

Below the main results from the first part of the thesis are summarised.

- SOSs and SQSs were generated. These smaller, 12 and 24 atom, cells approximates the correlations of larger cells. SQSs represent the random alloy case and SOSs represent thermodynamically representative structures.
- SRO parameter shows that PdAu:H can not accurately be described as a random alloy. Furthermore in the NN regime Pd-H and Au-V bonds are most common, while in second NN regime Pd-V and Au-H pairs are more prevalent.



# 3

## Electronic properties of PdAu:H

In this chapter the electronic properties of the special structures generated in the previous chapter will be studied. This is done in the DFT formalism. An introduction to DFT can be found in section 3.1. The special structures were relaxed using VASP [12] and subsequently the ground state electronic properties were calculated using GPAW [13–15]. The results can be found in section 3.2.

### 3.1 Introduction to density functional theory

In this section the most important theorems of DFT will be presented and discussed. The theorems by Hohenberg and Kohn will be introduced in the first subsection and in the second subsection the so-called Kohn-Sham ansatz will be presented.

In summary, Hohenberg and Kohn showed that the ground state properties of a many-body electron system only depend on the electron density. This is crucial since the number of spatial coordinates is reduced from  $3N$  to 3, where  $N$  is the number of electrons. The theorems by Hohenberg and Kohn do not solve the many-body electron problem but provide a useful reformulation of the problem.

Kohn and Sham proposed a method for solving this reformulated problem. Instead of solving the interacting many-body Schrödinger equation they assumed that one can instead solve a set of fictitious non-interacting Schrödinger-like equations that result in the same particle density.

All of the DFT calculations, in this thesis, are done within the Born-Oppenheimer approximation [16]. In summary the approximation separates the quantum me-

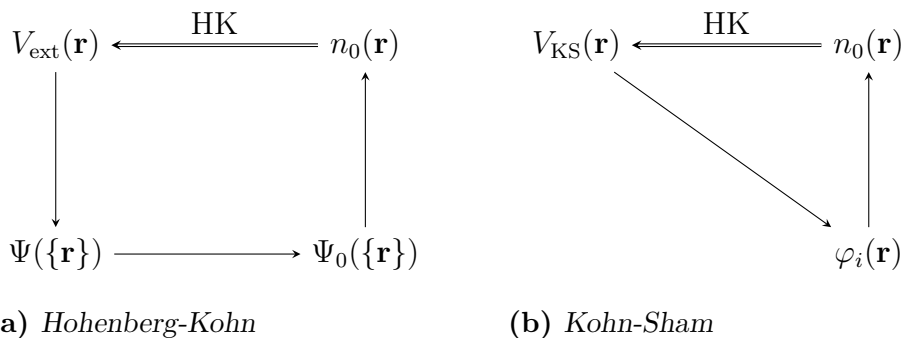


**Figure 3.1:** Hohenberg and Kohn showed that the electron density contains all ground state information. Kohn and Sham made DFT practical by replacing the interacting system as a non-interacting system in some potential,  $V_{KS}(\mathbf{r})$ .

chanical system of the cores and the electrons into two separate systems, that are independent of each other. Of course the position of the cores affects the electrons, but the dynamics of the cores does not affect the electronic system. Without being rigorous, the motivation behind this approximation is that the mass of the core is much larger than the electron mass, so one can assume that the electrons immediately are adjusted to the new position of the cores.

### 3.1.1 Hohenberg-Kohn theorems

The Hohenberg-Kohn theorems show that the energy of an electronic system can be expressed as a functional of the ground state electron density. In other words, the theorems translate the initial problem from a many-body wave function with  $3N$  spatial coordinates to a density of 3 spatial coordinates. Below the two Hohenberg-Kohn theorems are stated. They are directly cited from *Electronic Structure: Basic Theory and Practical Methods* [16].

**Theorem 1** *For any system of interacting particles in an external potential  $V_{\text{ext}}(\mathbf{r})$ , the potential  $V_{\text{ext}}(\mathbf{r})$  is determined uniquely, except for a constant, by the ground state particle density  $n_0(\mathbf{r})$ .*

**Corollary 1** *Since the Hamiltonian is thus fully determined, except for a constant shift of the energy, it follows that the many-body wave functions for all states (ground and excited) are determined. Therefore all properties of the system are completely determined given only the ground state density  $n_0(\mathbf{r})$ .*

**Theorem 2** *A universal functional for the energy  $E[n]$  in terms of the density  $n(\mathbf{r})$  can be defined, valid for any external potential  $V_{\text{ext}}(\mathbf{r})$ . For any particular  $V_{\text{ext}}(\mathbf{r})$ , the exact ground state energy of the system is the global minimum value of this functional, and the density  $n(\mathbf{r})$  that minimises the functional is the exact ground state density  $n_0(\mathbf{r})$ .*

**Corollary 2** *The functional  $E[n]$  alone is sufficient to determine the exact ground state energy and density. In general, excited states of the electrons must be determined by other means.*

This results in a translation from the many-body Schrödinger equation (in the Born-Oppenheimer approximation), see equation (3.1), to the functional form of the same problem,

$$E\Psi(\{\mathbf{r}\}) = [\hat{T}_e + \hat{V}_{e-e} + \hat{V}_{\text{ext}}] \Psi(\{\mathbf{r}\}), \quad (3.1)$$

where  $\hat{T}_e$  is the kinetic operator,  $\hat{V}_{e-e}$  the electron-electron interaction, and  $\hat{V}_{\text{ext}}$  is an externally applied potential. Often the external potential is simply the electron-ion interaction. The new form can be expressed as:

$$E[n] = T_e[n] + E_{e-e}[n] + \int d^3r V_{\text{ext}}(\mathbf{r})n(\mathbf{r})$$

$$n(\mathbf{r}) = |\Psi(\{\mathbf{r}\})|^2,$$

where the same naming convention has been used. By minimising this equation with respect to the electron density, the ground state energy is found and hence all other ground state properties. It should be noted that the functional  $T_e[n]$  as well as  $E_{e-e}[n]$  are in fact unknown, which is where the Kohn-Sham ansatz proves useful.

### 3.1.2 Kohn-Sham ansatz

In short, the Kohn-Sham ansatz is an approach that replaces the initial interacting many-body system with a non-interacting system. The assumption is that the initial electron density is equal to the density of this new non-interacting system. This new system can be expressed by independent equations where most electron-electron interactions are summed up into one exchange-correlation functional with respect to the density. One wishes that this interaction term, which must be approximated, has a small contribution to the total energy.

The total energy can be written as:

$$E_{\text{KS}}[n] = T_s[n] + \int d^3r V_{\text{ext}}(\mathbf{r})n(\mathbf{r}) + E_{\text{H}}[n] + E_{\text{xc}}[n]$$

$$n(\mathbf{r}) = \sum_i |\psi_i(\mathbf{r})|^2,$$

where  $T_s[n]$  is the non-interacting particle kinetic energy,  $E_{\text{H}}[n]$  is the classical density-density Coulomb interaction. The independent particle wave functions are denoted  $\psi_i(\mathbf{r})$ . The difference between the real, unknown, kinetic and density-density interaction and their fictitious counterparts is expressed in the exchange-correlation term:

$$E_{\text{xc}}[n] = \langle \hat{T} \rangle - T_s[n] + \langle \hat{V}_{e-e} \rangle - E_{\text{H}}[n].$$

This term is now the difficult part. There are various approximation to this term, such as the local density approximation and generalised gradient approximation. The single-particle Schrödinger-like equation, proposed by Kohn and Sham, is shown below:

$$\epsilon_i \psi_i(\mathbf{r}) = [\hat{T}_s + \hat{V}_{\text{H}} + \hat{V}_{\text{ext}} + \hat{V}_{\text{xc}}] \psi_i(\mathbf{r}) = [\hat{T}_s + \hat{V}_{\text{KS}}] \psi_i(\mathbf{r})$$

where the introduced potentials are functional derivatives:

$$\hat{V}_{\text{H}} = \frac{\delta E_{\text{H}}}{\delta n(\mathbf{r})}$$

$$\hat{V}_{\text{xc}} = \frac{\delta E_{\text{xc}}}{\delta n(\mathbf{r})}.$$

In practice, one solves these equations by making an initial guess of the Kohn-Sham (KS) orbitals,  $\psi_i(\mathbf{r})$ , which defines the particle density. Using this guess one evaluates the potentials. With the potentials the Hamiltonian is known and all of the orbitals can be calculated. One then uses these orbitals and repeats the process until the difference in particle densities, between two consecutive iterations, is below a judiciously chosen threshold.

## 3.2 Ground state density functional theory results

Ground state DFT was used to calculate the energies and wave functions of the non-interacting KS particles for various structures. By doing this one can visualise

the band structure and density of states (DOS) for the non-interacting system for all structures. This gives valuable information about what effect hydrogen has on the electronic properties of palladium-gold alloy and therefore on the optical properties. The density of state and band structures will be presented in subsections 3.2.3 and 3.2.2, respectively. The expansion of the Pd lattice due to gold and hydrogen will be presented in the following subsection.

### 3.2.1 Lattice expansion of the PdAu:H alloy

The SQSs (and SOSs) were relaxed using VASP with the vdW-DF-CX functional [17, 18]. The functional vdW-DF-CX was used due to its accurate prediction of lattice parameters [19]. The relaxation is crucial for the later calculations to be representative.

In Figure 3.2 the lattice parameter is shown for different gold concentrations as a function of hydrogen content. As expected hydrogen placed at interstitials of the palladium FCC lattice strains the lattice; gold has a similar effect. The lattice expansion was approximately 5% for a fully hydrogenated structure compared to a non-hydrogenated structure. Experimentally measured expansions typically show the trend  $(a_H^3 - a_0^3)/a_0^3 = 0.2c$  for  $\text{Pd}_{1-c}\text{H}_c$  [20]. The equivalent value predicted here was  $(a_H^3 - a_0^3)/a_0^3 \approx 0.15$  for the fully hydrogenated structure.

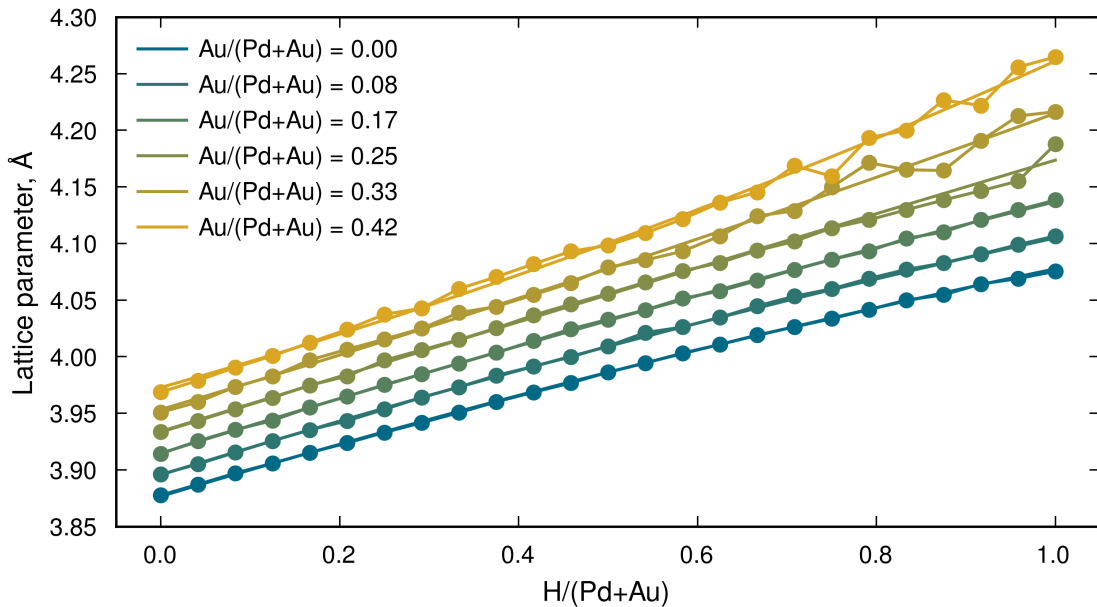


**Figure 3.2:** Lattice parameters for different gold and hydrogen content of the PdAu:H SQSs. The original FCC palladium lattice is expanded due to the introduction of gold and hydrogen. Fits are included that will be used in chapter 6 where the optical response of nanodisks will be studied.

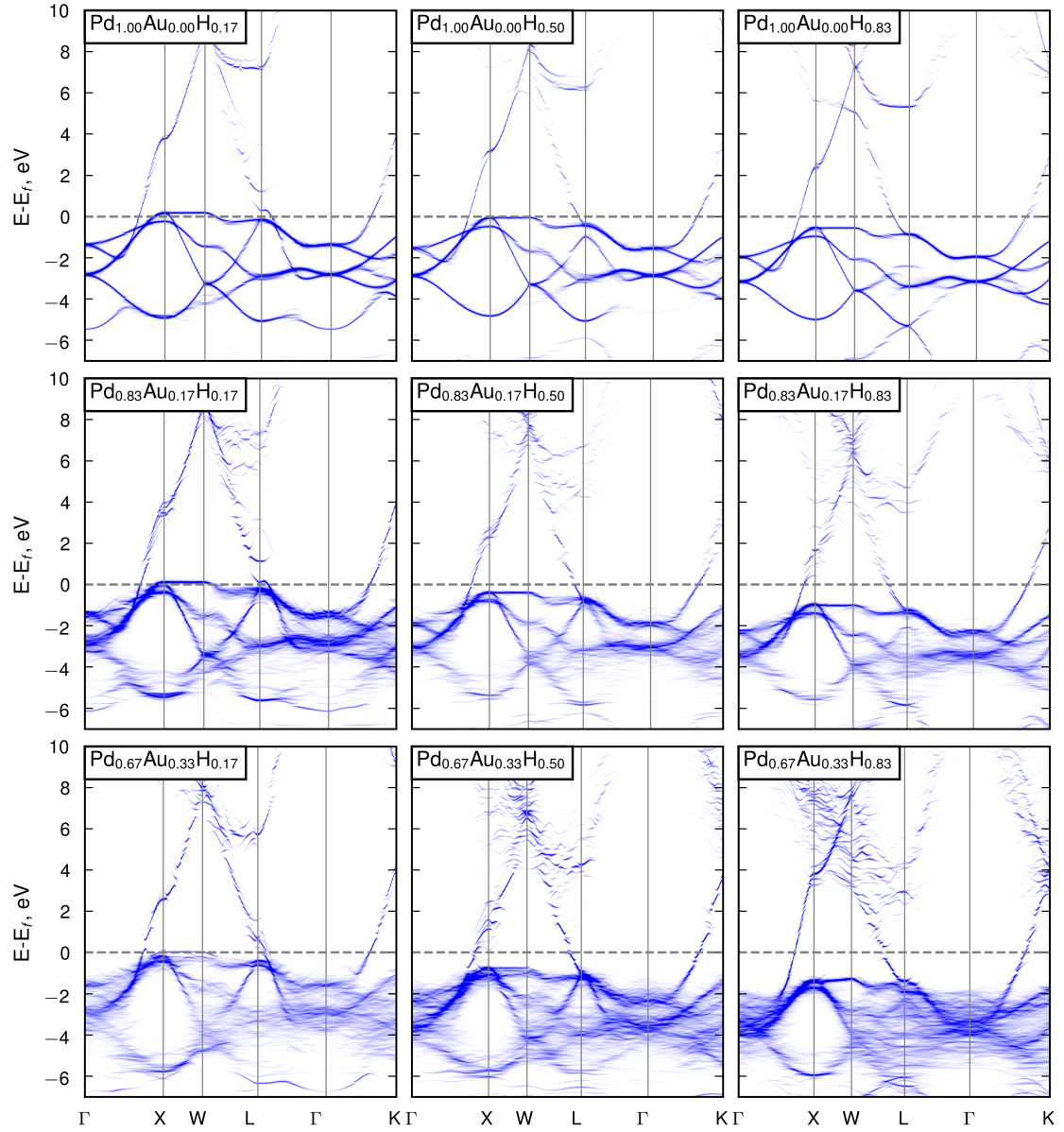


**Figure 3.3:** Unfolded band structures for some of the PdAu:H SQSs. The energies are relative to the Fermi level,  $E_f$ , and the high symmetry points of the  $k$ -space are marked on the  $x$ -axis. The band structures are unfolded onto the first Brillouin zone of the primitive Pd cell. A bigger overlap is visualised by sharp lines and the blurred lines indicates less overlap between the primitive and supercell band structures. Higher concentrations of H and Au results in the band close to the Fermi level being occupied and hence being pushed down below the Fermi level.

### 3.2.2 Band structure of PdAu:H

In the ground state DFT calculations the GLLB-SC functional [21] was used along with a plane wave basis set in GPAW. The motivation for using the GLLB-SC functional is that it captures the d-band behaviour well, which is crucial for the dielectric function and hence the optical spectrum. The d-band prediction is im-

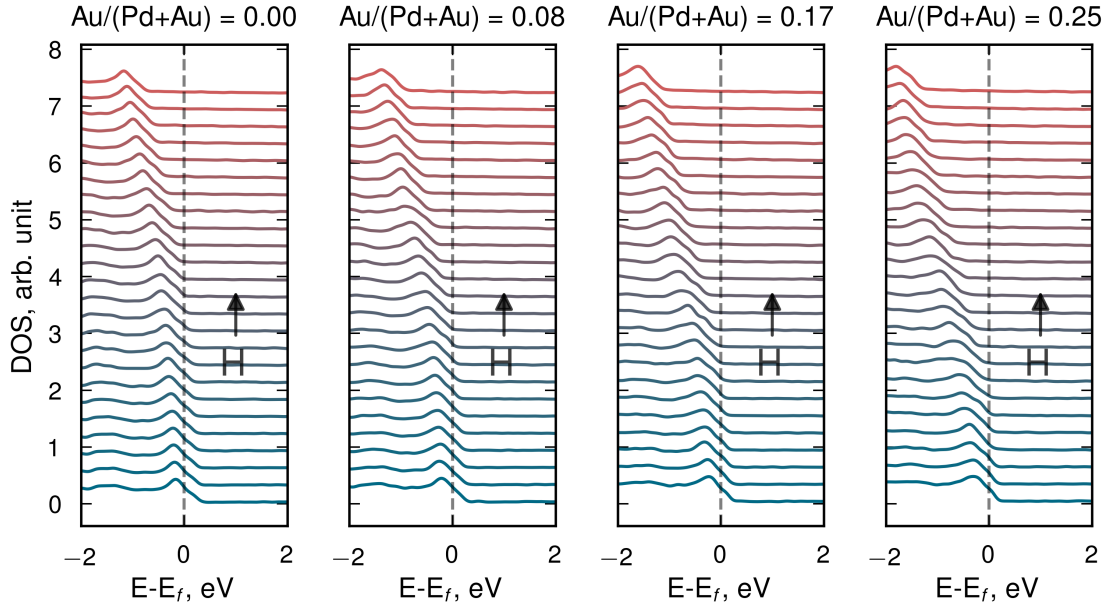


**Figure 3.4:** DOS for SQSs with up to 25% gold and hydrogen concentrations from 0% to 100% in steps of 4%. The figure shows that an increase in hydrogen concentration pushes the band below the Fermi level. An increase in gold concentration results in an earlier and more distinct effect. For all gold concentrations the effect of hydrogen concentration on the DOSs shift is weakly non-linear.

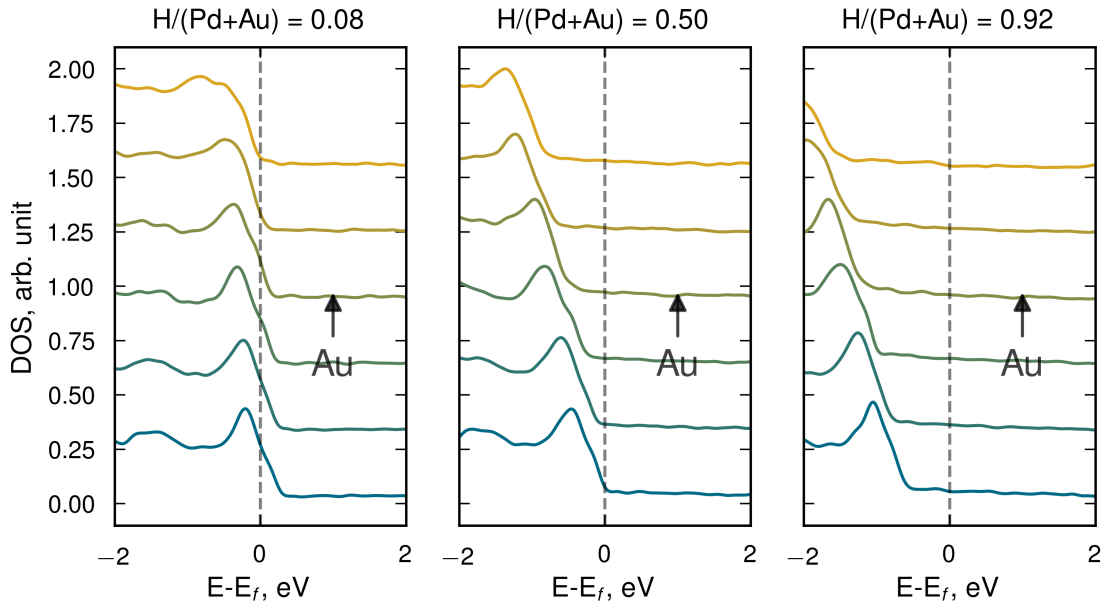


**Figure 3.5:** DOS as a function of gold concentrations from 0% to 42% with steps of 8% for three different hydrogen concentrations. An increase in the number of gold atoms results in the d-band edge being pushed down below the Fermi level. Adding more hydrogen atoms further enhances the effect, as seen in previous figures.

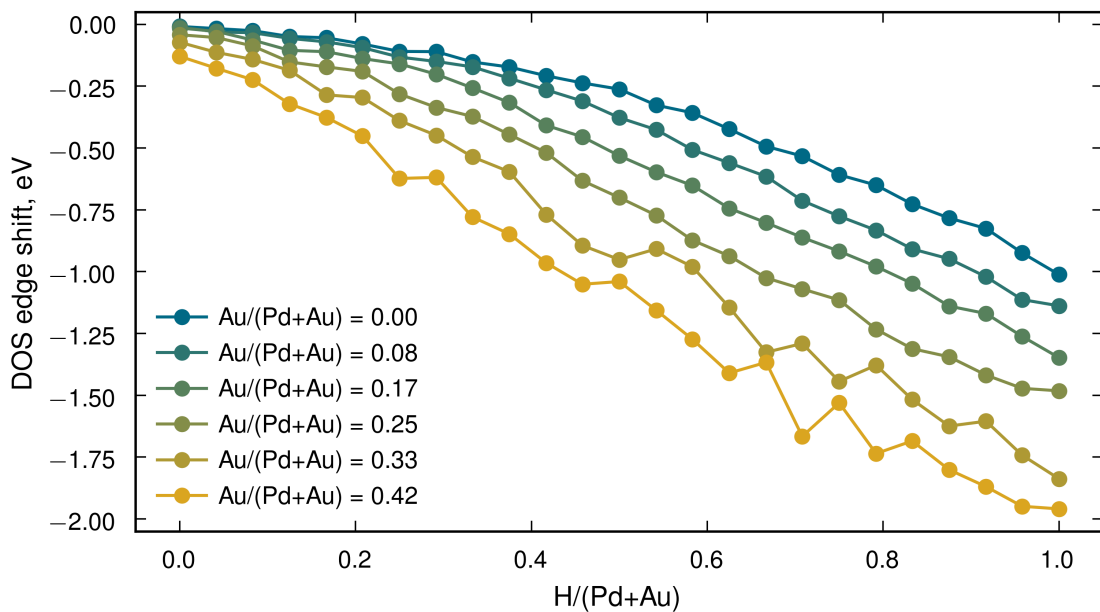


**Figure 3.6:** Shift in *d*-band edge with hydrogen for various gold concentrations for SQSs of the PdAu alloy. Interestingly the DOSs shift for  $Pd_{0.6}H_{0.4}$  and  $Pd_{0.58}Au_{0.42}$  relative to Pd is on the same order of magnitude.

portant since interband transitions give rise to peaks in the imaginary part of the dielectric function.

The resulting unfolded band structures for the SQSs for a few selected gold and hydrogen concentrations are plotted in Figure 3.3. Unfolding the band structure allows for easier comparison between the different supercells. In short unfolding means that the first Brillouin zone for the supercell is mapped onto the bigger first Brillouin zone of a primitive cell that is the reference system. Here the unfolding is done from PdAu:H to the primitive cell of Pd. The transparency of the lines is proportional to how well the states of the supercell contribute to the states of the primitive cell. As expected with higher Au concentration there is less overlap between the supercell and the primitive Pd cell. Furthermore it can be clearly seen that with more hydrogen the *d*-like states in the vicinity of the Fermi level,  $E_f$ , is pushed below the Fermi level, i.e. adding hydrogen results in filling of the bands close to the Fermi level. Increasing the gold concentration has a similar effect of pushing down the band below the Fermi level.

### 3.2.3 Electronic density of states of the alloy

In Figure 3.4 the DOS for SQSs with Au concentrations up to 25% is presented. Each subfigure shows the DOSs for a Au concentration with H concentrations ranging from 0% to 100%, with steps of circa 4%. It can be seen that increasing the hydrogen concentration results in the *d*-band being increasingly occupied and slowly being pushed below the Fermi level. This trend is shifted to smaller H concentrations with an increase in gold concentration.

The DOSs for fixed hydrogen concentrations is presented in each subfigure of figure

3.5. This is done to visualise the effect of an increase in gold concentration on the DOSs shift. Gold concentrations from 0 % to 42 % are shown with steps of 8 %. As shown in the previous figure, an increase in gold concentration pushes the d-band further down below the Fermi level.

In Figure 3.6 the position of the d-band edge relative to the Fermi level is visualised as a function of hydrogen content. Here the definition of the *edge* is arbitrarily set to a value that result in a point in the middle of the d-band edge. This was done to further highlight the fact that introduction of hydrogen in PdAu alloys pushes down the d-band relative to the Fermi level. Furthermore, adding hydrogen to pure palladium results in filling of the d-band. Adding gold to palladium shifts this effect to smaller hydrogen concentrations.

The interpretation is the following: the d-band in pure palladium is not fully occupied, i.e. the d-band crosses the Fermi level. On the other extreme is gold. The d-band edge of gold is circa 2 eV below the Fermi level. Alloying Pd with Au then pushes down the d-band due to the larger number of valence electrons from gold. Introducing hydrogen in Pd (and PdAu alloys) pushes down the d-band similarly.

### 3.3 Summary

The key points from this chapter are presented below.

- The PdAu:H SQSs and SOSs were relaxed with DFT and a reasonable agreement with experimental lattice parameters was found.
- Alloying palladium with hydrogen shifts the d-band below the Fermi level. This effect is enhanced when alloying with gold.

# 4

## Dielectric response of PdAu:H

In this chapter the dielectric response of the alloy will be analysed. This is done by using time-dependent density functional theory (TDDFT) and the ground state DFT calculations discussed in the previous chapter. More specifically, linear response TDDFT will be applied using the software GPAW [15]. A short introduction to the theory will first be presented followed by a convergence study. In section 4.3 the calculated dielectric functions (DFs) will be shown and analysed.

### 4.1 Introduction to time-dependent DFT

For studying excitations in systems, such as optical absorption, one must go further than the traditional ground state density functional theory. This stems from the discrepancy between the KS eigenstates and the real electronic eigenstates. In other words, a possible optical excitation energy is not equal to the difference in the highest occupied KS orbital and the lowest unoccupied KS orbital.

To calculate the dielectric response the TDDFT formalism has been used. The Runge-Gross theorem is essential in TDDFT [22]. It is similar to the Hohenberg-Kohn theorems since it allows one to study a time-dependent Schrödinger equation by moving into the density picture. The theorem states that the density determines the external potential, similarly to the static counterpart. Hence all other observables can be expressed by this time-dependent density.

Here, KS orbitals are also introduced to turn the complex many-body system into a more approachable set of non-interacting systems that result in the same density.

#### 4.1.1 Linear response and dielectric function

This subsection aims to shed light at how the response of a quantum mechanical many-body system can be calculated using TDDFT. First the density response will be shown in the linear response limit. Then the DF will be expressed from this density response. In this section it is assumed that the system is probed by a weak time-dependent potential,  $\delta V_{\text{ext}}(\mathbf{r}, t)$ , on top of the original external potential (typically originating from the ions in the system).

In linear response theory the deviation from the initial ground state density is:

$$\delta n(\mathbf{r}, \omega) = \int d^3r' \chi(\mathbf{r}, \mathbf{r}', \omega) \delta V_{\text{ext}}(\mathbf{r}', \omega), \quad (4.1)$$

where  $\chi(\mathbf{r}, \mathbf{r}', \omega)$  is the density-density linear response function in frequency domain. It essentially explains how the density in point  $\mathbf{r}$  is affected by a perturbation in  $\mathbf{r}'$ .

The density can also be expressed in the KS response function:

$$\delta n(\mathbf{r}, \omega) = \int d^3 r' \chi_{\text{KS}}(\mathbf{r}, \mathbf{r}', \omega) \delta V_{\text{KS}}(\mathbf{r}', \omega) \quad (4.2)$$

$$\delta V_{\text{KS}}(\mathbf{r}, \omega) = \delta V_{\text{ext}}(\mathbf{r}', \omega) + \int d^3 r' \frac{1}{|\mathbf{r} - \mathbf{r}'|} \delta n(\mathbf{r}', \omega) + \int d^3 r' f_{xc}(\mathbf{r}, \mathbf{r}', \omega) \delta n(\mathbf{r}', \omega),$$

where  $\delta V_{\text{KS}}(\mathbf{r}, \omega)$  is the variation in the dynamic KS potential due to the weak perturbation. Here, the exchange-correlation kernel,  $f_{xc}(\mathbf{r}, \mathbf{r}', \omega)$ , is introduced:

$$f_{xc}(\mathbf{r}, \mathbf{r}', \omega) = \mathcal{F} \left[ \frac{\delta V_{xc}[n](\mathbf{r}, t)}{\delta n(\mathbf{r}', t)} \Big|_{n=n_{GS}} \right],$$

where  $\mathcal{F}$  denotes the Fourier transform. Under the assumption that the KS system results in the same response as the real many-body system, i.e. the assumption that equation (4.1) is equal to equation (4.2), one can derive the Dyson-like equation that couples the two density response functions:

$$\chi(\mathbf{r}, \mathbf{r}', \omega) = \chi_{\text{KS}}(\mathbf{r}, \mathbf{r}', \omega) + \int d^3 r'' \int d^3 r''' \chi_{\text{KS}}(\mathbf{r}, \mathbf{r}'', \omega) K(\mathbf{r}'', \mathbf{r}''', \omega) \chi(\mathbf{r}''', \mathbf{r}', \omega),$$

where  $K(\mathbf{r}'', \mathbf{r}''', \omega)$  is the sum of the Hartree and exchange-correlation kernels. This equation can be written, by introducing abbreviations for the integrals, in the more compact form:

$$\chi = (\mathbf{1} - \chi_{\text{KS}} \star K)^{-1} \star \chi_{\text{KS}}.$$

This expression shows that the density response of the full interacting many-body system can be calculated from the ground state KS density response. Note, that this is true as long as the kernel  $K$  is known, which in general is not the case.

The KS response in reciprocal space takes the form [23, 24]:

$$\chi_{\mathbf{G}, \mathbf{G}'}^{\text{KS}} = \lim_{\eta \rightarrow 0^+} \frac{1}{V} \sum_{n, n', \mathbf{k}} \frac{f_{n' \mathbf{k} + \mathbf{q}} - f_{n \mathbf{k}}}{\epsilon_{n' \mathbf{k} + \mathbf{q}} - \epsilon_{n \mathbf{k}} - \omega - i\eta} \cdot \langle \psi_{n' \mathbf{k} + \mathbf{q}} | e^{i(\mathbf{q} + \mathbf{G}) \cdot \mathbf{r}} | \psi_{n \mathbf{k}} \rangle \langle \psi_{n \mathbf{k}} | e^{i(\mathbf{q} + \mathbf{G}') \cdot \mathbf{r}} | \psi_{n' \mathbf{k} + \mathbf{q}} \rangle,$$

where  $f_i$  denotes the occupation number of orbital  $i$ ,  $\epsilon_i$  the energy of the orbital,  $\psi_i$  the wave function of the orbital. The indices  $n$  and  $\mathbf{k}$  represents the band number and the  $k$ -point of the state. Incoming photon wave vector is denoted  $\mathbf{q}$ . A term in the sum is small if the two states have the same occupation number or if the overlap between the two orbitals is low. For an excitation to occur the difference in energy between the two states must be on the same magnitude as the incoming photon energy,  $\omega$ .

In this thesis the many-body response will be approximated using the random phase approximation (RPA). This is done with the motivation that the difference in response between RPA and higher order kernels (such as the adiabatic local density approximation) is small for metals [25]. RPA treats the difficult dynamic exchange-correlation part in the kernel by neglecting said effects. In other words, the exchange-correlation kernel is  $f_{xc} = 0$  and hence the complete kernel,  $K$ , can be written in the form [26]:

$$K_{\mathbf{G}, \mathbf{G}'}^{\text{RPA}}(\mathbf{q}) = \frac{4\pi}{|\mathbf{q} + \mathbf{G}|^2} \delta_{\mathbf{G} \mathbf{G}'} + \cancel{f_{xc}}$$

With this approximation and the information of the ground state KS system the response of the many-body system can be evaluated. The true response can be seen as the combination of the non-interacting response and some additional corrections described by the kernel.

The density response is useful since it contains information about the (microscopic) DF. Using the RPA mentioned above the DF takes the form [22]:

$$\epsilon_{\mathbf{G},\mathbf{G}'}^{\text{RPA}}(\mathbf{q},\omega) = \delta_{\mathbf{G}\mathbf{G}'} - \frac{4\pi}{|\mathbf{q} + \mathbf{G}|^2} \chi_{\mathbf{G},\mathbf{G}'}^{\text{KS}}(\mathbf{q},\omega)$$

Everything in the equation above is known from the KS system. The macroscopic DF, i.e. the quantity that relates the external field with the induced field in the solid, can be written:

$$\epsilon_M(\hat{\mathbf{q}},\omega) = \lim_{\mathbf{q} \rightarrow \mathbf{0}} \frac{1}{\epsilon_{\mathbf{0},\mathbf{0}}^{-1}(\mathbf{q},\omega)}.$$

Here also the optical limit is taken ( $\mathbf{q} \rightarrow \mathbf{0}$ ). The imaginary part of this quantity corresponds to the optical absorption in a solid. Therefore, by evaluating this quantity for the solid under investigation one can get information about optical processes in the material.

## 4.2 Convergence of TDDFT parameters

To achieve accurate and physically sound optical spectra the needed DFs need to be independent of the specific values of computational parameters. In other words, the DF should be converged with respect to parameters such as broadening parameter, number of bands, cutoff energy in response calculation, and  $k$ -space density. Increasing the number of grid points and bands will obviously improve the accuracy but also increase the computational cost. Therefore a trade-off between accuracy and cost must be achieved. This section aims at finding reasonable values to the parameters listed above.

The cutoff energy,  $E_c$ , defines the size of the plane wave basis set used in the TDDFT calculation. It determines the size of the dielectric matrix  $\epsilon_{\mathbf{G},\mathbf{G}'}$ . A higher cutoff energy results in a bigger dielectric matrix.

In the ground state DFT calculation both the number of bands,  $N_{\text{bands}} = N_b N_{\text{electrons}}/2$ , and the number of  $k$ -points in each Cartesian direction,  $N_k$ , are crucial parameters. Here,  $N_{\text{electrons}}$  denotes the number of valence electrons and  $N_b$  is a scalar sampled between 1.4 and 2.4 in this study. Higher  $k$ -point density results in improved accuracy in the energy states while an increased number of bands allows for higher energy excitations. Increasing the number of  $k$ -points *ad infinitum* will not be valuable.

In Figure 4.1 the DF of Pd<sub>12</sub>H is presented for a few different values on the parameters discussed above. From the figure it can be seen that the cutoff energy has little to no effect on the DF. A larger broadening parameter,  $\eta$ , smears out the details of the peak, both making the peak lower and wider, which is expected from a broadening parameter. In other words, increasing  $\eta$  results in earlier convergence but the accuracy of the DF is reduced. As expected, more bands above the Fermi

level leads to additional higher energy excitations. Note, however, that as a result of the Kramer-Kronig relation the number of bands does affect the lower energies in the *real* part of the DF. This is significant since according to Mie theory in the electrostatic approximation the absorption of a metallic sphere is high when  $\text{Re}\{\epsilon\} \approx 2$ . This could result in a shift of the absorption peak of up to 0.5 eV, as indicated by the dashed line in the second column of the third row in Figure 4.1. A too low  $k$ -point density results in a noisy DF. For this system 11 points, in each direction, appear to be enough for a converged DF.

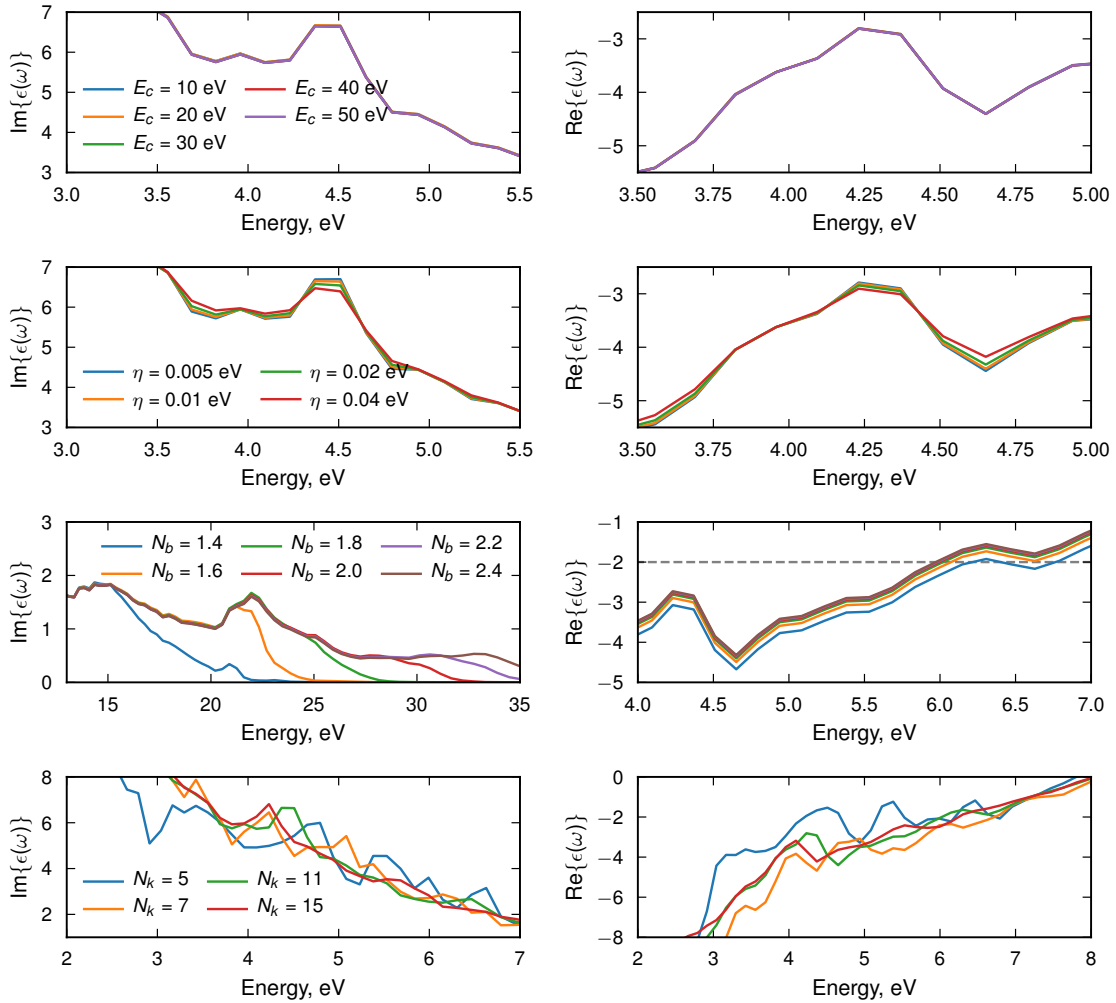


**Figure 4.1:** Convergence of DF with computational parameters. Imaginary (left) and real part (right) of the DF. The studied system is Pd<sub>12</sub>H. It can be seen in the first row that the cut off energy in the TDDFT calculation is not so important. The broadening parameter,  $\eta$ , has a slightly bigger impact but at 0.01 eV the DFs seem to converge. The number of bands, parametrized by  $N_b$ , affects the higher end of the imaginary part of the DF. Note however that the real part is dependent on the number of bands at low energies, even down to 4 eV and lower. The number of gridpoints in  $k$ -space affects both the imaginary and real part of the DF. At 11 points on each x,y and z axis most of the noise is removed from the DFs.

The most crucial parameters used in the ground state and time-dependent DFT calculations are shown in Table 4.1.

Parameter	$N_k$	$N_b$	$E_c$	$\eta$
Value	11	1.8	40 eV	0.01 eV

**Table 4.1:** The most crucial parameters that were used in the ground state and time-dependent DFT calculations. The number of bands and  $k$ -points affect the ground state calculation while the cut off energy and broadening parameter are introduced in the response calculation.

### 4.3 Dielectric response of PdAu:H

In this section the DF for the PdAu:H alloy is presented for various gold and hydrogen concentrations. This is done using the formalism described above.

A typical set of DFs with varying hydrogen content is presented in Figure 4.2. Here, only Pd<sub>0.75</sub>Au<sub>0.25</sub>:H is shown but similar trends were observed for other gold concentrations. It can be difficult to interpret these plots, but it is apparent that hydrogen pushes the real part of the DF to lower energies. This trend seems to be (approximately) monotonic. The imaginary part decreases at lower energies due to hydrogenation, this typically affects the shape of the extinction peak of a nanoparticle.

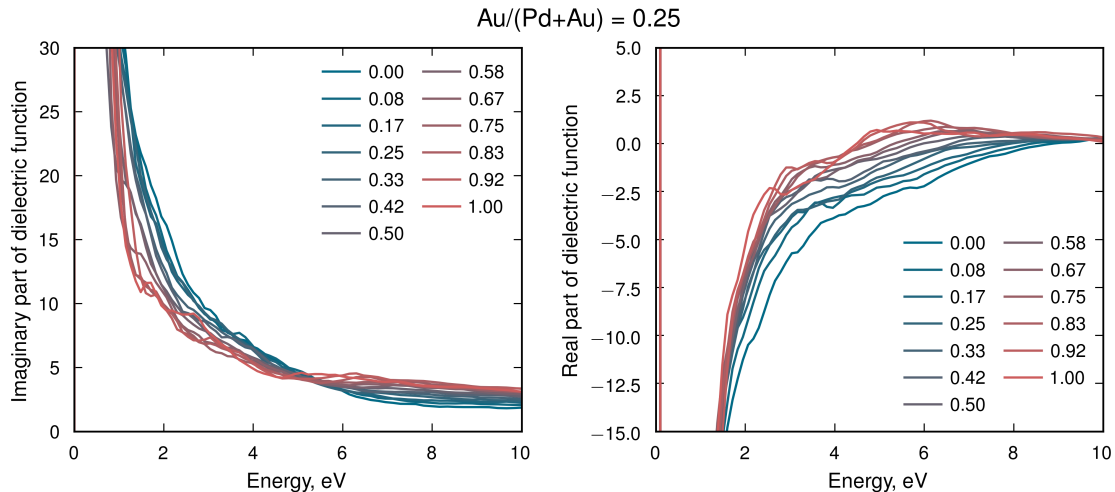


**Figure 4.2:** DFs for Pd<sub>0.75</sub>Au<sub>0.25</sub>:H with various hydrogen concentrations. Higher hydrogen content is denoted with a more red line and the numbers in the legend correspond to hydrogen content. The imaginary part increases due to hydrogenation at around 8 eV while it decreases in the visible regime circa 2 eV. The real part is pushed to lower energies due to hydrogenation. Similar trends were found for other gold concentrations.

In Figure 4.3 the loss function,  $-\text{Im}\{1/\epsilon\}$ , for Pd<sub>1-x</sub>Au<sub>x</sub>H<sub>y</sub> SQSs are shown. The loss function is used here since it conveniently “hides” the divergent Drude peak

#### 4. Dielectric response of PdAu:H

at low energies, which otherwise dominates the picture. Typically a higher loss function results in higher probability of exciting plasmons in bulk materials. From the figure it can be seen that the peak is shifted to lower energies with higher hydrogen content. When gold is introduced the peaks are flattened, but the peaks are still being red-shifted with increasing hydrogen content.

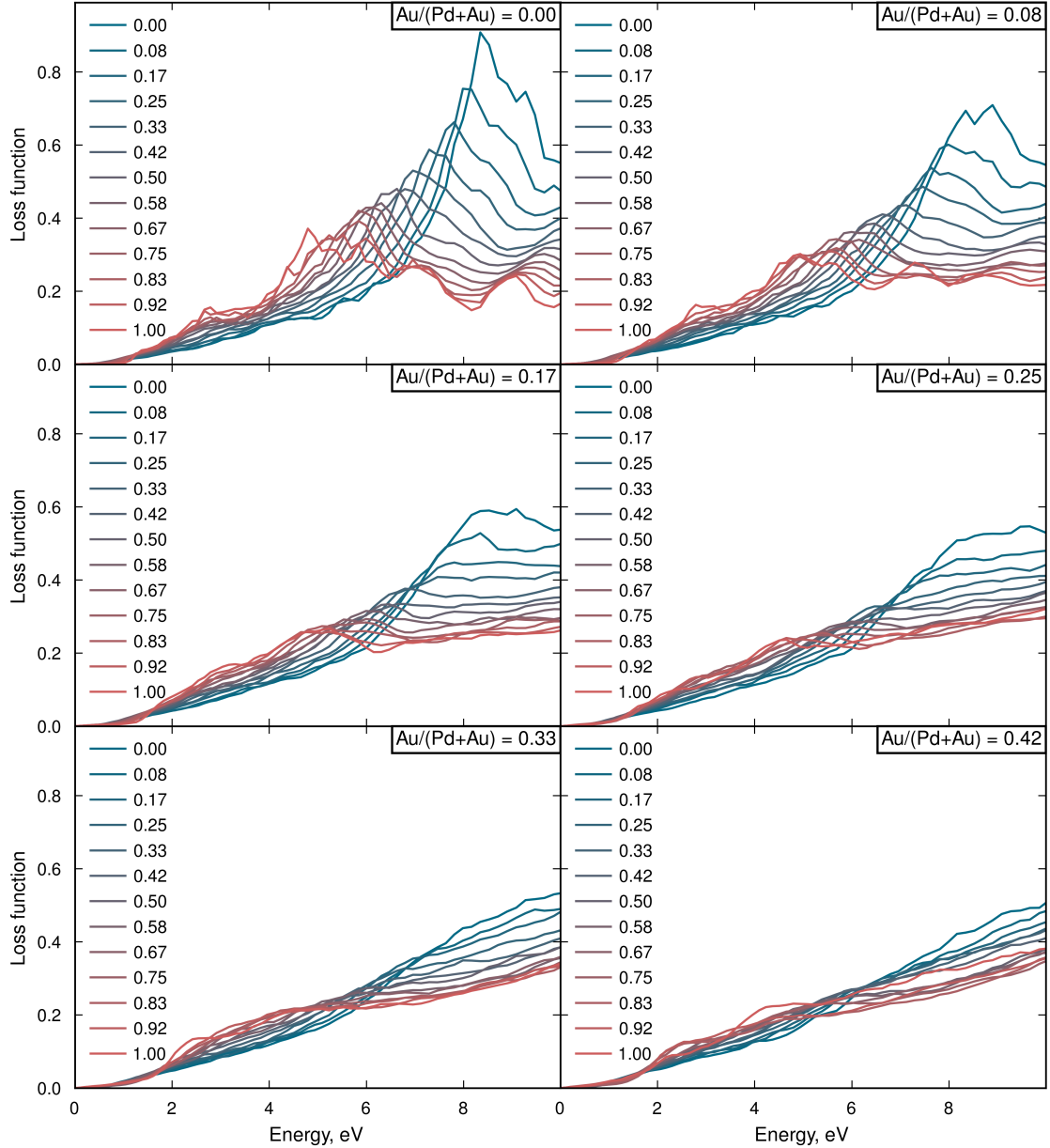


**Figure 4.3:** Loss functions of SQS PdAu:H alloys. The different subplots represents different gold contents and a more red coloured line corresponds to a higher hydrogen concentration.

In Figure 4.4 the loss function for SQS Pd<sub>0.75</sub>Au<sub>0.25</sub>:H is shown together with its SOS counterpart. Note that these SOSs have 12 metal atoms, compared to the SQSs that are constructed with 24 metal atoms. The trends are similar in the two cases in the sense that the peak is red-shifted with hydrogen. The similarity between SQSs and

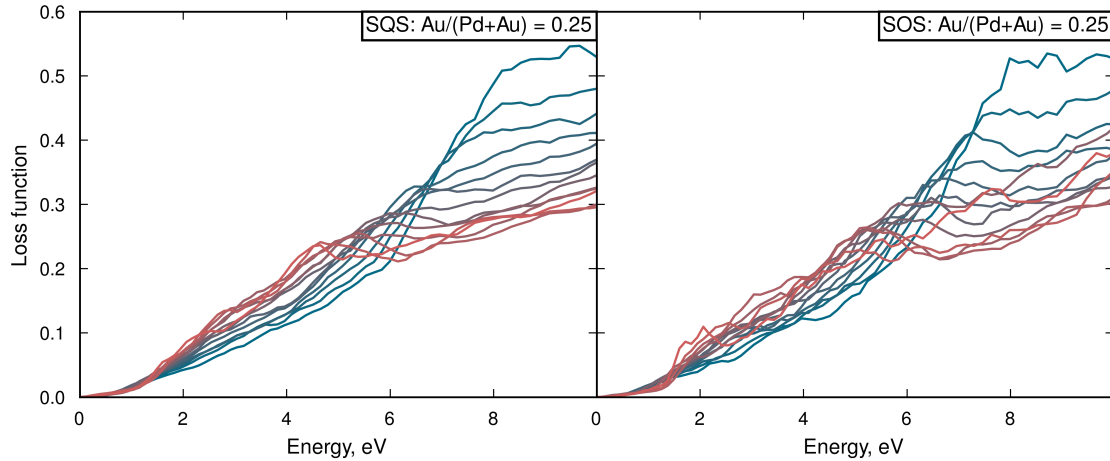


**Figure 4.4:** A comparison between the loss functions for SQS and SOS cases of  $\text{Pd}_{0.75}\text{Au}_{0.25}:\text{H}$ . A more red coloured line correspond to higher hydrogen concentration. The red-shift is similar for the two cases.

SOSs indicates that the response is not strongly affected by microscopical ordering of the alloys.

The figures above show the loss function from 0 to 9 eV. In applications the interesting interval is near the visible regime, i.e. about 1.5 to 3 eV. The loss functions in this regime are shown in Figure 4.5. Interestingly, the loss functions for Pd:H and  $\text{Pd}_{0.75}\text{Au}_{0.25}:\text{H}$  are quite similar as a function of hydrogenation. This is promising in so far as it could result in similar optical response for palladium and palladium-gold alloys. Of course the relation between the loss function and the optical spectra is not trivial, but this at least makes it reasonable to expect a monotonic response with hydrogenation for both Pd and  $\text{Pd}_{0.75}\text{Au}_{0.25}$ .

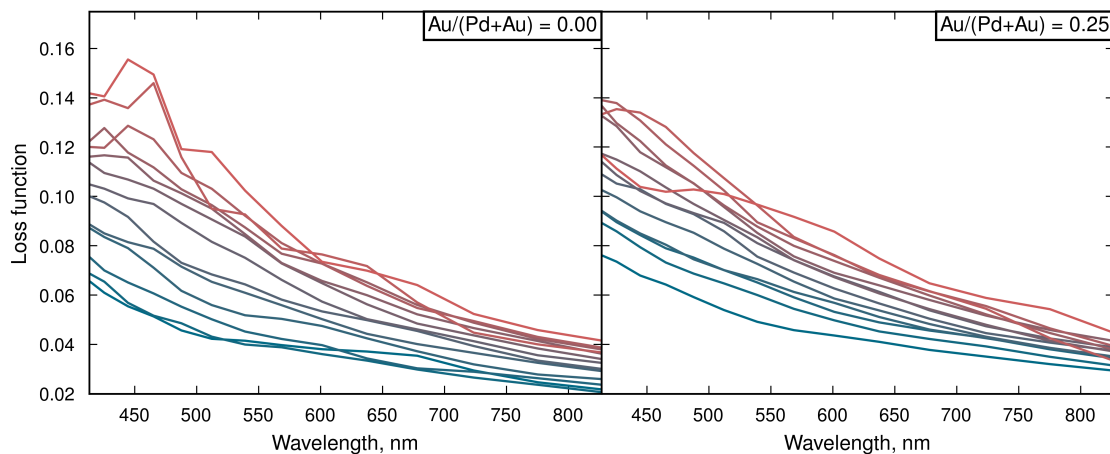


**Figure 4.5:** Visible regime of the SQS loss functions. Here the energy is converted to wavelength. Only two gold concentrations are shown, but interestingly the difference between the two cases is quite small in this regime. An almost monotonic change due to hydrogenation is seen.

In Figure 4.6 constant-energy slices of the real part of the DF for Pd:H are presented as a function of hydrogen content. Electrostatic Mie resonances occur at energies that correspond to specific values of the real part of the DF. The specific resonance criteria can be altered by varying shape (and size) of the nanostructure. In the figure this would result in a vertical shift of the dashed line. It can be seen that in the short wavelength regime the real part is almost constant with respect to hydrogen, this would result in a very small shift in optical resonance peak due to hydrogenation. By contrast, in the long wavelength regime the response should be substantially larger. This also opens up the possibility of altering the magnitude of the response by changing particle shape and size. This phenomena is shown in Figure 6.13. In the figure the sensitivities are shown as a function of initial absorption peak position, which was altered by changing the shape of the nanostructure. The sensitivity is defined as the ratio between the peak shift and the hydrogen concentration.

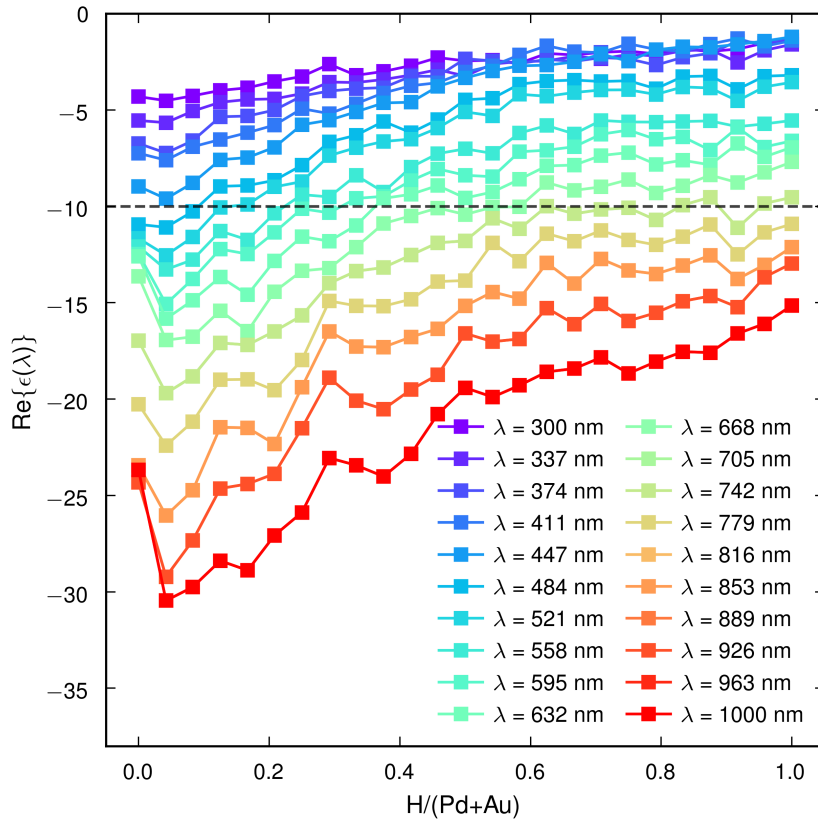


**Figure 4.6:** Slices of the real part of the DF for Pd:H with varying hydrogen content. From the figure it can be seen the (optical) resonance peak might shift in different ways depending on what regime one is probing. The dashed line represents a hypothetical resonance criteria, that may be changed by varying the shape of the nanostructure. If the UV-regime is probed it is likely that the shift is small, if at all existing, while in the IR-region a small change in concentration results in a much larger shift.

## 4.4 Summary

The main results from this chapter are:

- DFs for SQSs and SOSs were calculated within the linear response TDDFT formalism.
- The loss function of PdAu alloys red-shifts with hydrogenation. The loss function curve flattens with increasing gold content. The red-shift is monotonic.
- In the visible regime the response due to hydrogenation is similar for Pd and Pd<sub>0.75</sub>Au<sub>0.25</sub>.
- The real part of the DF behaves differently during hydrogenation in different regimes of the visible regime. This should lead to different responses depending on which energy regime is probed, where the latter is determined by the geometry of the nanostructure.



# 5

## Lorentzian representation of dielectric functions

The DF from TDDFT must be transformed to a form that is suitable for electromagnetic simulations. In this thesis, such simulations have been carried out using the MEEP package [27], which requires a representation of the DF via Lorentzian oscillators. The transformation of the DF into a series of Lorentzians is the focus of this chapter. In the first section the fitting method is presented and then some fitting examples are shown in the subsequent section.

A visual summary of the fitting method is shown in Figure 5.1. The principal idea is that an initial basis set of Lorentzians is created. Then a regularisation algorithm is used to select the most important Lorentzians from this set. A final fine tuning of the parameters that enter said Lorentzians is carried out by using a non-linear least squares method. Ideally the resulting set of Lorentzians is small and approximates the raw data well.

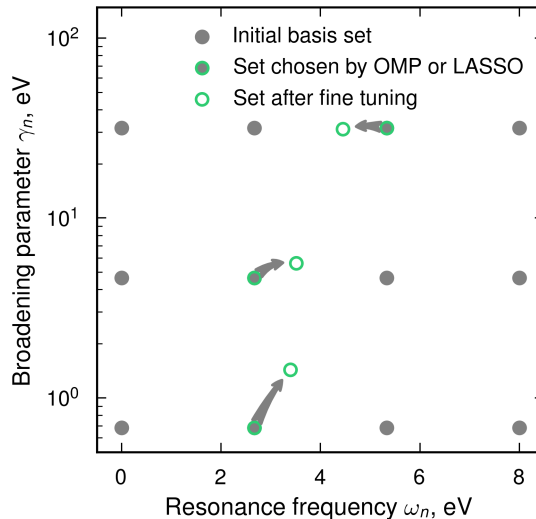


**Figure 5.1:** Overview of fitting method. Grey circles denotes the initial basis set of Lorentzian functions. Green circles on top of grey circles represent the functions selected by orthogonal matching pursuit (OMP) or least absolute shrinkage and selection operator (LASSO). The grey arrows indicate the fine tuning of the parameters  $\gamma_n$  and  $\omega_n$ , this is done by a non-linear least squares method. The final Lorentzians are the hollow green circles.

## 5.1 Fitting method

The electromagnetic simulation software MEEP expects the DF of dispersive materials to be represented as a sum of Lorentzians. Therefore the DFs from the TDDFT calculations, here referred to as the raw data  $\epsilon_r(\omega)$ , must be fitted to this form. The requested function is of the form:

$$\begin{aligned}\epsilon(\omega) &= \epsilon_\infty + \sum_{n=1}^N \frac{x_n \omega_n^2}{\omega_n^2 - \omega^2 - i\omega\gamma_n} = \epsilon_\infty + \sum_{n=1}^N x_n L_n(\omega) = \\ &= \epsilon_\infty + \mathbf{x} \cdot \text{Re}\{\mathbf{L}(\omega)\} + i\mathbf{x} \cdot \text{Im}\{\mathbf{L}(\omega)\},\end{aligned}$$

where  $\epsilon_\infty$  is the instantaneous response. The parameters  $x_n$ ,  $\omega_n$  and  $\gamma_n$  represent strength, resonance frequency, and broadening of oscillator  $n$ . By separating the real and imaginary part, the fitting problem takes the form:

$$\begin{cases} \text{Re}\{\epsilon_r\} - \epsilon_\infty & \approx \mathbf{x} \cdot \text{Re}\{\mathbf{L}(\omega)\} \\ \text{Im}\{\epsilon_r\} & \approx \mathbf{x} \cdot \text{Im}\{\mathbf{L}(\omega)\} \end{cases}$$

Since the raw data is discretised with respect to frequency the problem can be seen as a standard matrix equation,  $\mathbf{b} \approx \mathbf{A}\mathbf{x}$ . Here,  $\mathbf{b}$  is a vector containing the real part of the DF concatenated with the imaginary part. The functions  $L_n(\omega)$  are stored as rows in  $\mathbf{A}$ , where each row correspond to one of the sampled frequencies. Note here that the upper/lower half of the matrix correspond to the real/imaginary part of the functions  $L_n(\omega)$ .

By making a two-dimensional grid of Lorentzians,  $L_n(\omega)$ , with different resonance frequencies and broadening values it is straightforward to solve this problem. The result is the optimal strengths for these oscillators. For this method to work as intended the number of oscillators would have to be large, i.e. the grid should be densely sampled. This is, however, impractical since each additional oscillator increases the computational cost of the electromagnetic simulation.

We are thus faced with the task of solving an underdetermined problem where the number of samples is smaller than the number of variables. As a reference, the number of sampled frequencies is roughly 100 while the number of Lorentzians is on the order of 10,000. We seek a so-called sparse solution to the underdetermined linear equation at hand and thereby obtain a good representation of the data with as few Lorentzians as possible. This task can be achieved using different regularisation techniques.

OMP is the algorithm of choice in this thesis. The algorithm finds solutions to problems of the type:

$$\mathbf{x}_{\text{sparse}} = \arg \min_{\mathbf{x}} \|\mathbf{b} - \mathbf{A}\mathbf{x}\|_2^2 \text{ subject to } \|\mathbf{x}\|_0 \leq N_{\text{req}},$$

where  $N_{\text{req}}$  is the hyperparameter that specifies how sparse the solution should be [28]. In other words, if the user specifies  $N_{\text{req}} = 5$  the final fit will contain 5 Lorentzian oscillators. A big advantage of OMP compared to other regularisation techniques, such as LASSO and elastic-net, is the fact that the hyperparameter itself

is intuitive. In practice OMP was applied by using the tool HIPHIVE [29] that in turn calls functions from scikit-learn<sup>1</sup>.

For reference, the LASSO objective function is the following:

$$\mathbf{x}_{\text{sparse}} = \arg \min_{\mathbf{x}} \|\mathbf{b} - \mathbf{A}\mathbf{x}\|_2^2 + \alpha \|\mathbf{x}\|_1.$$

LASSO thus solves the least squares problem while penalising solutions that are larger in magnitude. Here the hyperparameter is  $\alpha$  and if set to zero one recovers the ordinary least-squares problem.

The sparse solution  $\mathbf{x}_{\text{sparse}}$  yields the optimal strengths for the defined grid of oscillators. To further improve the values of the resonance frequencies and broadening of the resulting, OMP selected, oscillators a non-linear least-squares method<sup>2</sup> was applied. This can be seen as a fine tuning of the parameters.

From the perspective of computational cost, it is tempting to force the number of oscillators to be low. However, from a physical perspective this can be contraindicated since valuable information is lost. To deal with this issue the Bayesian information criterion (BIC) and the Akaike information criterion (AIC) were used. These measures allow one to strike a balance between fitting error and the number of variables in the model [30].

$$\text{BIC} = N_s \ln(\text{MSE}) + N_p \ln(N_s) + c$$

$$\text{AIC} = N_s \ln(\text{MSE}) + 2N_p + c$$

Here,  $N_s$  is the number of samples, i.e. the number of frequencies in the problem at hand,  $N_p$  is the number of parameters, and MSE is the mean-square error of the fit. The value  $c$  is a constant for a data set and a fitting model, i.e. the quantities can only be compared relative to each other for the same data set and fitting model.

In Figure 5.2 the BIC and AIC values are shown for the OMP and adaptive-LASSO fitting methods. Adaptive-LASSO is similar to LASSO but weights are included in the penalisation. Here both OMP and adaptive-LASSO were paired with non-linear least squares optimisation. As seen in the figures, the minimum BIC values correspond to a reasonable trade off between error and number of oscillators.

A further motivation, in addition than computational cost, for decreasing the number of oscillators is *overfitting*. An increase in the number of oscillators might decrease the fit error but rather than capturing further physical features this will reproduce features in the DFs that are due to numerical convergence. Including too many oscillators will then lead to artefacts in the resulting optical spectra as seen in Figure 5.3, which shows the absorption and scattering spectra for a sphere of radius 50 nm revealing small oscillations due to the overfitting of the dielectric function.

**To summarise:** OMP in combination with non-linear least-squares optimisation was used, where the hyperparameter  $N_{\text{req}}$ , which determines the number of oscillators, was selected by minimising the BIC.

<sup>1</sup><https://scikit-learn.org/stable/>

<sup>2</sup>[https://docs.scipy.org/doc/scipy/reference/generated/scipy.optimize.least\\_squares.html](https://docs.scipy.org/doc/scipy/reference/generated/scipy.optimize.least_squares.html)

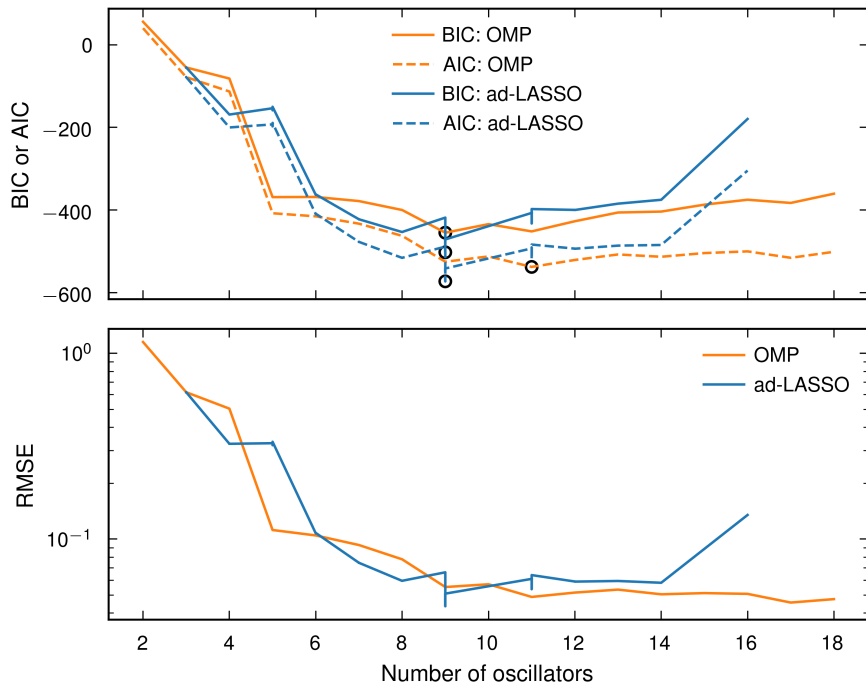


**Figure 5.2:** Proof of concept of the fitting methods in combination with information criteria. In the upper figure BIC and AIC are shown as a function of the number of oscillators. minima are marked with black circles. Both OMP and adaptive-LASSO show good results. OMP was chosen in this thesis since it is easier to use.

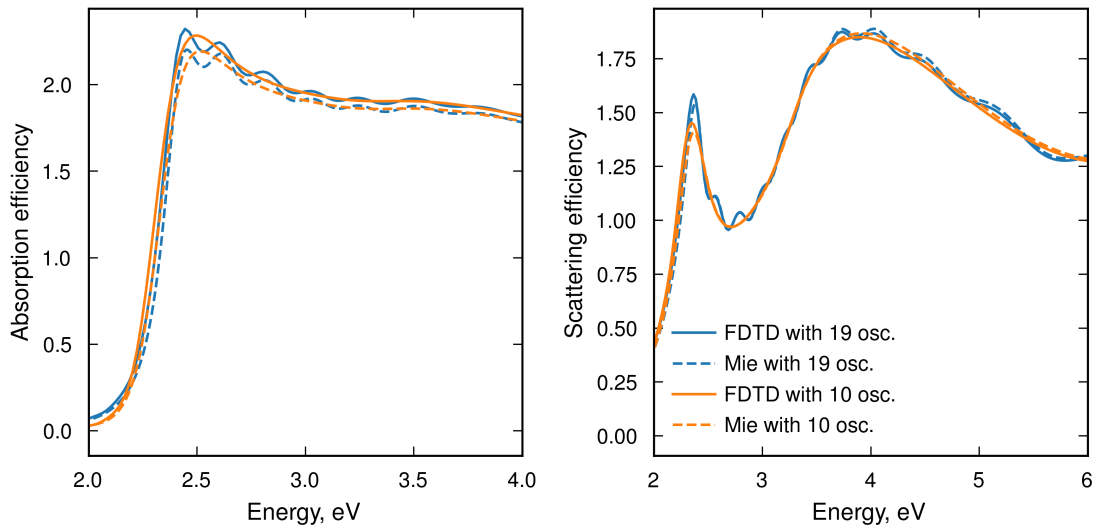


**Figure 5.3:** Optical spectra for a gold sphere with radius 50 nm. A comparison is done between two different fits and also between Mie theory and data generated with finite-difference time-domain (FDTD) simulations. Too many Lorentzians in the fit introduce small oscillations in the resulting spectra. In general the agreement between Mie theory and simulation is good, although the height of the peak differ slightly.

## 5.2 Examples of Lorentzian fits

This section presents typical fits obtained using the methods mentioned above. In Figure 5.4 the calculated DF for  $\text{Pd}_{0.75}\text{Au}_{0.25}\text{:H}$  is shown together with two different fits. The difference between the two fits is the maximum number of oscillators allowed. The fits are very good, even with fewer than 6 oscillators for the lower hydrogen concentrations. At higher concentrations of hydrogen the sharp details cannot be described with only 6 oscillators. It should be kept in mind that in practice the very high hydrogen concentrations are not as interesting as the mid to low concentration regime.

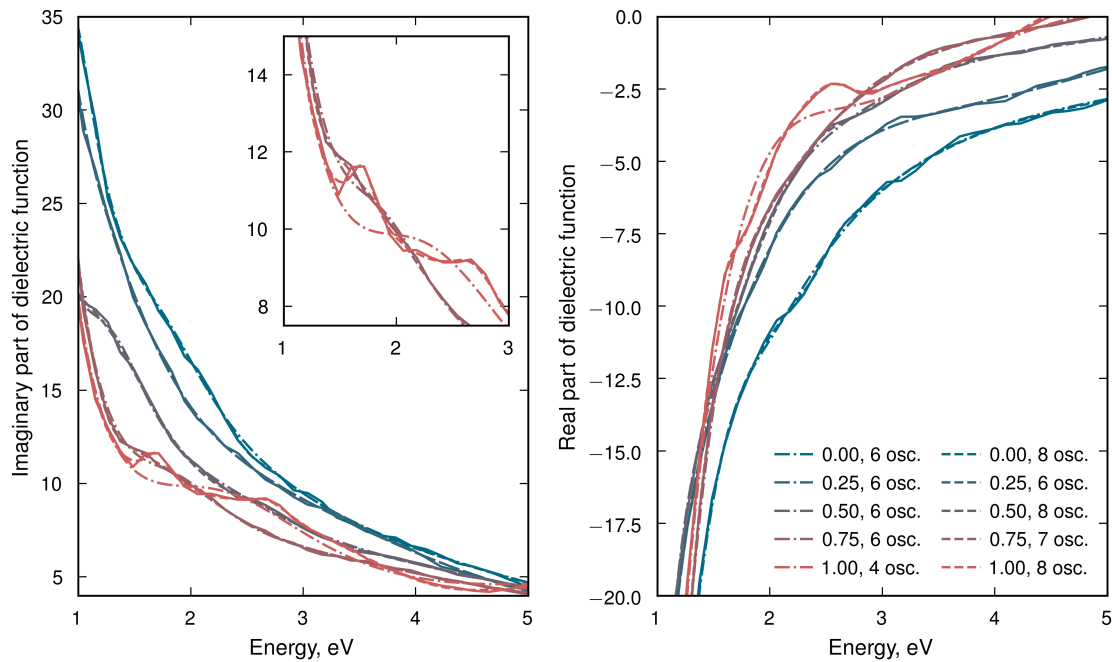
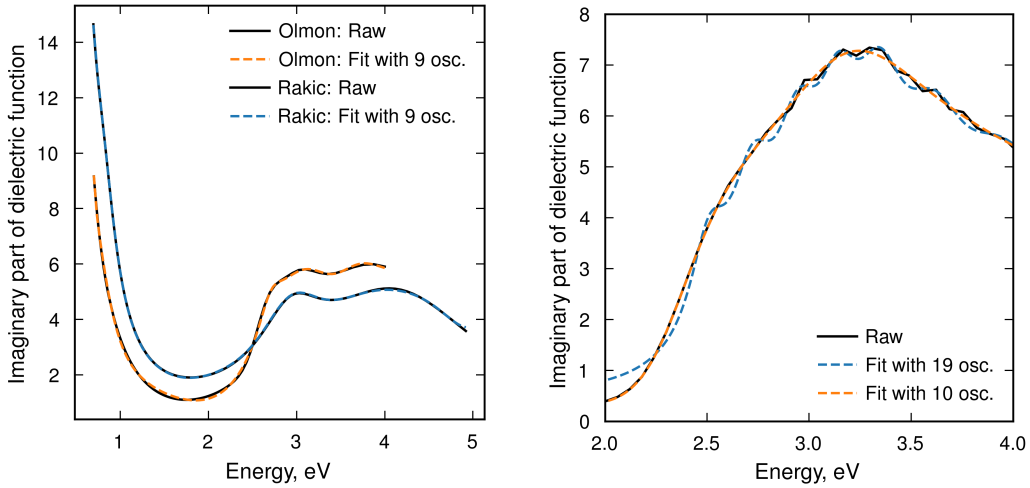


**Figure 5.4:** Typical fitting scenarios of some DFs. It is clear that for hydrogen concentrations up to 75% only 6 oscillators are needed. Overall the fitting methods are working as expected.

Even though the fits with a maximum of 6 oscillators are not optimal in the high hydrogen content regime, the fits are overall good. This is especially true if one compares with experimentally obtained DFs, where different measuring techniques can result in a very wide range of values. Such a comparison is done in Figure 5.5. The experimental gold DFs were measured by Olmon *et al.* [31] and Rakic *et al.* [32]. The figure illustrates that even if the fits would be non-ideal the difference in experimental data is often much larger than the errors introduced in these types of fits.



(a) Experimental data and resulting fits. (b) Classical overfitting problem.

**Figure 5.5:** To the left: The imaginary part of the DF for gold from experimental measurements by Olmon *et al.* and Rakic *et al.* Included in the plot are the fits generated using the presented method. To the right: The imaginary part of the dielectric function for gold with two different fits. Small oscillations can be seen if too many oscillators are included.

### 5.3 Summary

The most important results from this chapter are:

- A fitting method was developed that converts the TDDFT dielectric function to the Lorentzian form expected by MEEP.
- In short the method relies on regression with regularisation for selecting the most suitable Lorentzians from a large initial basis set. Then a fine tuning of the parameters  $\gamma_n$  and  $\omega_n$  and the strengths of the oscillators is performed by a non-linear least squares method. This whole procedure is done using a variable number of oscillators, i.e. the hyperparameter  $N_{\text{req}}$  was varied. Then the value that minimises BIC was chosen for that DF.
- This was successfully done for all DFs from the TDDFT calculations.

# 6

## Optical response of PdAu:H nanodisks

The optical response of a nanoparticle is a convolution of the properties the underlying material and the geometry and shape of the particle. The material property relevant here is the DF, a bulk property, which in this thesis was obtained through TDDFT calculations.

In this thesis the optical response will be calculated using the FDTD electromagnetic software MEEP [27]. By defining a region described by the DF for a specific PdAu:H alloy, one can calculate the optical extinction spectra for that geometry with that bulk property. Doing this for all hydrogen concentrations one obtains the optical spectra as a function of hydrogenation. This chapter hence bridges the gap between the DF and a measurable optical quantity.

In this chapter the sensor is always, unless specified otherwise, a truncated cone with angle  $\theta = 60^\circ$ , see Figure 6.1. The sensor is placed on top of a silica substrate modelled with a constant refractive index  $n = 1.47813$ .

The basic theory is described in the first section. This is followed by a short convergence study and the subsequent sections present the ultimate results of this thesis.

### 6.1 Finite-difference time-domain method

In classical electromagnetism Maxwell's equations describe the interaction between the electric and magnetic fields. Furthermore the equations describe the interaction between these fields and matter itself. The macroscopic Maxwell's equations can be written as:

$$\begin{aligned}\nabla \cdot \mathbf{D} &= \rho_f \\ \nabla \cdot \mathbf{B} &= 0 \\ \nabla \times \mathbf{E} &= -\frac{\partial \mathbf{B}}{\partial t} \\ \nabla \times \mathbf{H} &= \mathbf{J}_f + \frac{\partial \mathbf{D}}{\partial t},\end{aligned}$$

where  $\mathbf{E}$ ,  $\mathbf{H}$ , and  $\mathbf{J}_f$  are the electric field, magnetic field, and the free current density, respectively. The displacement field and magnetic flux density are denoted  $\mathbf{D} = \epsilon \mathbf{E}$  and  $\mathbf{B} = \mu \mathbf{H}$ . In the macroscopic Maxwell's equations only the free charge density,  $\rho_f$ , is considered.

By solving these equations for a given system, including the material and a source, one can gain knowledge about how much of the electromagnetic power from the source is absorbed or scattered in the material. There are different ways of solving these equations, and in this thesis the FDTD method will be used to solve Maxwell's equations in time domain. This is profitable since FDTD makes it possible to study a broad frequency response with only one simulation.

In FDTD the derivatives, spatial and temporal, in Maxwell's equations are approximated with finite differences. In other words, the space and time coordinates are discretised and then the simulation is propagated by taking small steps in time. The size of the timestep and the grid cell must satisfy the Courant condition [33]. The Courant condition can be expressed as  $\Delta t/\Delta x < n/\sqrt{D}$ , where  $\Delta t$  and  $\Delta x$  are the timestep and the dimension of the spatial grid cell,  $n$  is the smallest refractive index and  $D$  is the dimension of the system.

The goal is to calculate the absorption and scattering from the disk-and-substrate system and the essential steps are described here. The software stores the time-dependent fields through defined flux surfaces and then evaluates the Fourier transform of these fields. One can then calculate the (transmitted) power through a surface as:

$$P(\omega) = \text{Re}\left\{\hat{n} \cdot \int d^2\mathbf{x} \mathbf{E}_\omega^*(\mathbf{x}) \times \mathbf{H}_\omega(\mathbf{x})\right\}.$$

By doing this calculation on all sides surrounding the system and taking the sum of all sides one obtains the total absorbed power (here directions are very important). Normalising this quantity with the incoming intensity yields the absorption cross section  $\sigma_{abs}$ . The intensity is the radiated power divided by the area of the flux region above the disk,

$$\sigma_{abs} = \frac{P(\omega)}{I(\omega)}.$$

The scattering cross section,  $\sigma_{scat}$ , can be calculated in a similar fashion but now the incident fields must be subtracted before calculating the power through the different surfaces. Also a sign change is needed since absorption corresponds to the power *into* the volume while scattering is defined via the flux *out of* the volume. The dimensionless absorption and scattering efficiencies are evaluated as:

$$Q_{abs} = \frac{\sigma_{abs}}{A},$$

where  $A$  is the area of the disk as seen from the point-of-view of the source.

In practice a reference calculation is first done with only the silica substrate. The intensity from the source is stored as well as the incident fields. As mentioned before the intensity is needed for normalisation in the expression of the cross sections and the incident fields must be subtracted when the scattered power is calculated.

In Figure 6.1 the computational cell is shown. The source is a Gaussian-pulse source with a defined width and centre frequency and is coloured red in the figure. The electric and magnetic fluxes are calculated through a flux region, which is the blue coloured box in the figure. To simulate an infinite system perfectly matched layers (PMLs) are placed around the system. PMLs are designed to absorb all incoming radiation without reflecting any power back into the cell.

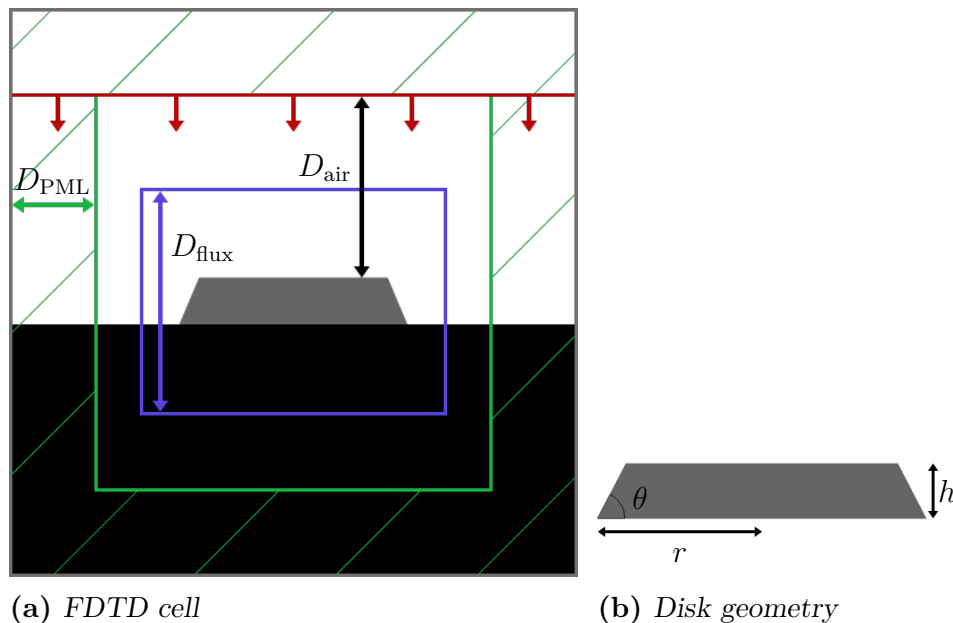


**Figure 6.1:** Illustration of the computational FDTD cell and the sensor. In the figure to left the green area represents the PML and the red line shows the location of the Gaussian source. The blue line indicates the flux region, i.e. the surface through which the electromagnetic flux is calculated. There must be enough vacuum in between the flux region and the source, which essentially puts a limit on  $D_{\text{air}}$ . The sensor is placed on top of the silica substrate shown as the black region in the figure. The sensor to the right illustrates the definitions of height, radius, and angle. When calculating the geometrical cross-section  $A$  the (larger) radius of the base is used.

## 6.2 Convergence and performance of MEEP

This section is aimed to present and motivate the parameters used in the electromagnetic FDTD simulation. Computational cost and scaling of the software will also be presented. The purpose of the study is to obtain estimates of parameter values that balance cost vs accuracy.

In Figure 6.2 the effect of three important FDTD parameters on the computed optical spectra is shown. Here, the studied system is the truncated cone on a silica substrate. The vacuum and PML thickness as well as the resolution of the computational cell are being varied and then height, position, and full width at half maximum (FWHM) of the absorption and scattering peak are examined. This was done for three different systems: pure gold, pure palladium and the alloy Pd<sub>90</sub>Au<sub>10</sub>.<sup>1</sup> From the figure it can be seen that the thickness of the PML layer and the amount of vacuum surrounding the disk is crucial. However, the spectra are barely affected by these parameters as long as they are kept above roughly 100 nm.

The spatial (and thereby the temporal) resolution is more intricate. Here the change in the spectra is much slower, but at a resolution of roughly  $500 \mu\text{m}^{-1}$  the height,

<sup>1</sup>These DFs can be found in the alloy DF database: [https://sharc.materialsmodeling.org/alloy\\_dielectric\\_functions/](https://sharc.materialsmodeling.org/alloy_dielectric_functions/)

position, and FWHM of the peak are converged. Even if there is a small change between  $500 \mu\text{m}^{-1}$  and  $600 \mu\text{m}^{-1}$  for a specific material, the changes are of similar magnitude for the different materials. It should be noted that the height of the scattering peak for Au (line without dots in top right figure) does not exhibit the same trend as for the other materials. In other words, the spectra are converged, relative to each other, with a resolution of  $500 \mu\text{m}^{-1}$  with the exception of possibly the height of the scattering peak.

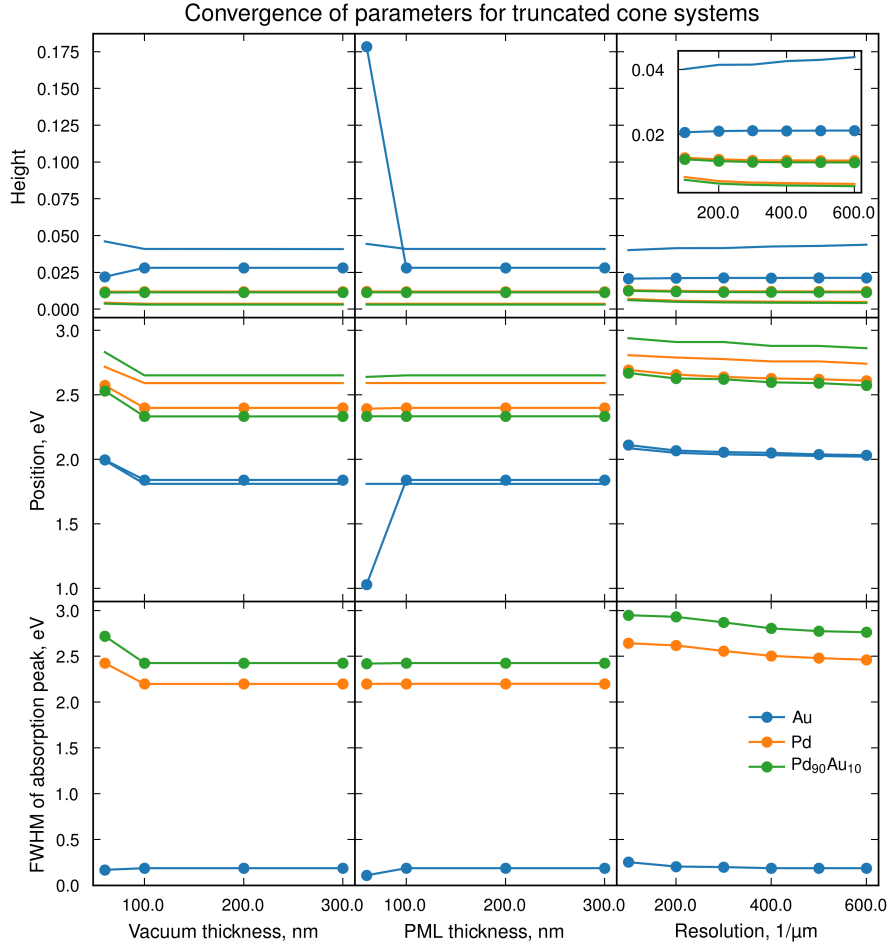


**Figure 6.2:** Height, position and FWHM of the absorption and scattering peaks. The lines with dots correspond to absorption values. As a summary: the spectra are converged, relative to each other, if one uses vacuum and PML thickness of 100 nm and a resolution of  $500 \mu\text{m}^{-1}$ .

A keen eye probably notices that the peak position is not the same if one compares the calculation series with varying PML thickness (and vacuum thickness) and the series with varying resolution. The reason for this is that the resolution used in the thickness series was set to  $160 \mu\text{m}^{-1}$ . The difference is still surprisingly large, and the reason for the large discrepancy is connected to how the spatial grid is discretised. This is illustrated further in Figure 6.3. For simplicity only the peak position is shown, but the same trends can be seen in peak height and FWHM. A periodicity of  $100 \mu\text{m}^{-1}$  can be seen here and if one looks at the heights of the

peaks a periodicity of  $50 \mu\text{m}^{-1}$  can also be seen (not shown here). The fact is that the discretisation of the cell is dependent on resolution and for different values the discretisation algorithm results in different geometries of the nanodisk. For example, when increasing the resolution from  $140 \mu\text{m}^{-1}$  to  $150 \mu\text{m}^{-1}$  the resulting nanodisk has a drastically different height and therefore the optical peaks are shifted. By increasing the resolution a lot the difference between these geometries decreases.

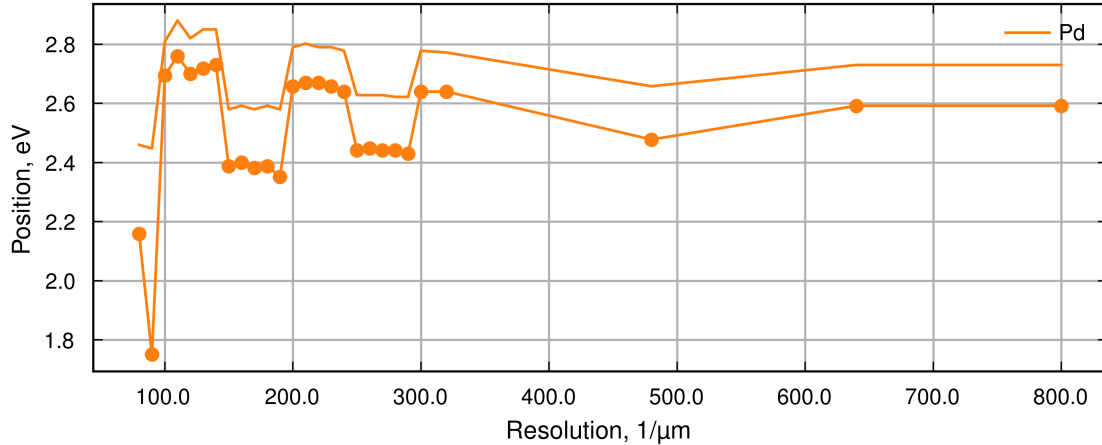


**Figure 6.3:** *Finely sampling different resolutions show that the resulting discretised cell generates different “versions” of the nanodisk. Here two different versions are detected that have a slightly different optical peak position. Increasing the resolution results in a smaller difference between the geometries, as expected.*

Increasing the resolution and thickness parameters *ad infinitum* is not practical due to the increased computational cost. This is illustrated in Figure 6.4 where the wall time divided by the simulation time is shown for different values of resolution and vacuum thickness. The ratios are also normalised with the number of oscillators in the Lorentzian fit of the DF for every material. As expected the cost scales, roughly, by the fourth power with respect to resolution and linearly with respect to vacuum thickness. Note that increasing the resolution increases both the spatial and temporal resolution, hence the expected fourth power instead of third power. Ideally the speedup of the wall time scales linearly with the number of cores. This would require the software to be fully parallelizable which is not realistic. In Figure 6.5 the speedup for the MEEP software is shown. The speedup is defined as  $t_1/t_N$ , where  $t_i$  is the wall time when  $i$  cores are used. All of these timings were done under the same conditions, with only the number of cores varying. At roughly 16 cores the gain of using additional cores is minimal. In the bottom subfigure the actual wall time normalized with the simulation time in MEEP units, m.u., is also shown.

Given the result of the convergence, cost, and scaling study the parameters for the production runs were chosen. They are presented in Table 6.1.

## 6. Optical response of PdAu:H nanodisks

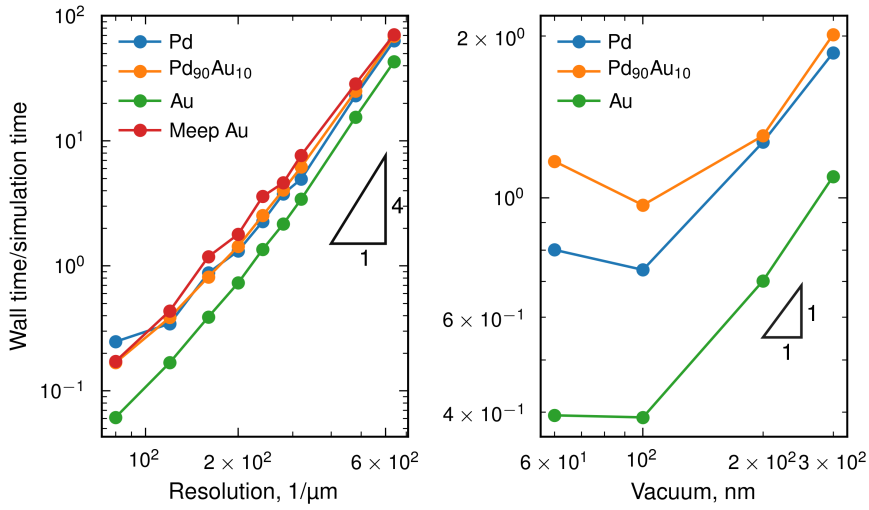


**Figure 6.4:** Wall time, in seconds, divided by the simulation time, in MEEP units. This ratio is normalised to the number of oscillators in the DF. The cost scales, roughly, as a fourth power with respect to resolution and linearly with vacuum thickness.

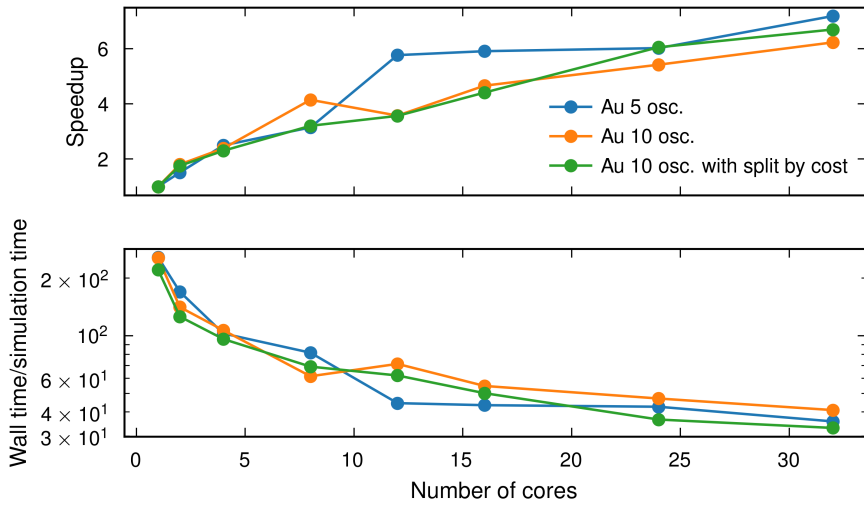


**Figure 6.5:** Upper figure shows the speedup of the MEEP simulations with respect to number of cores. These times were produced under strong scaling conditions. In the bottom figure the wall time in seconds is divided by the MEEP simulation time. For reference the simulation time in MEEP units for these calculations were circa 15 m.u., which roughly results in  $60 \text{ s/m.u.} \times 15 \text{ m.u.} = 15 \text{ min}$  with 16 cores.

**Table 6.1:** Parameters for MEEP production runs.

Parameter	Vacuum thickness	PML thickness	Resolution	Number of cores
Value	100 nm	100 nm	$500 \mu\text{m}^{-1}$	16

### 6.3 Absorption or scattering

Depending on application, it can be desirable to achieve a higher absorption than scattering efficiency, or vice versa. This choice is mainly informed by the measurement setup and the purpose of the device. To decide the size of the truncated nanocone, absorption and scattering spectra were studied as a function of height and diameter of the disk as shown in Figure 6.6. The peak efficiencies are red-shifted with increasing disk size. Increasing the size of the disk results in a higher scattering efficiency, while the absorption efficiency exhibits a maximum at a height of 20 nm. From this point onward the disk height was set to 20 nm, unless specified otherwise, since this results in maximum absorption efficiency. Another benefit of using the specified size is that the peak position is on the order of  $2.7 \text{ eV} \approx 460 \text{ nm}$ , which is in the blue region of the optical spectrum. Later in this chapter it will be shown that introduction of hydrogen red-shifts the peak and therefore it is crucial that the non-hydrogenated case is not too far to the red end of the spectra, if the readout should be close to the visible range.

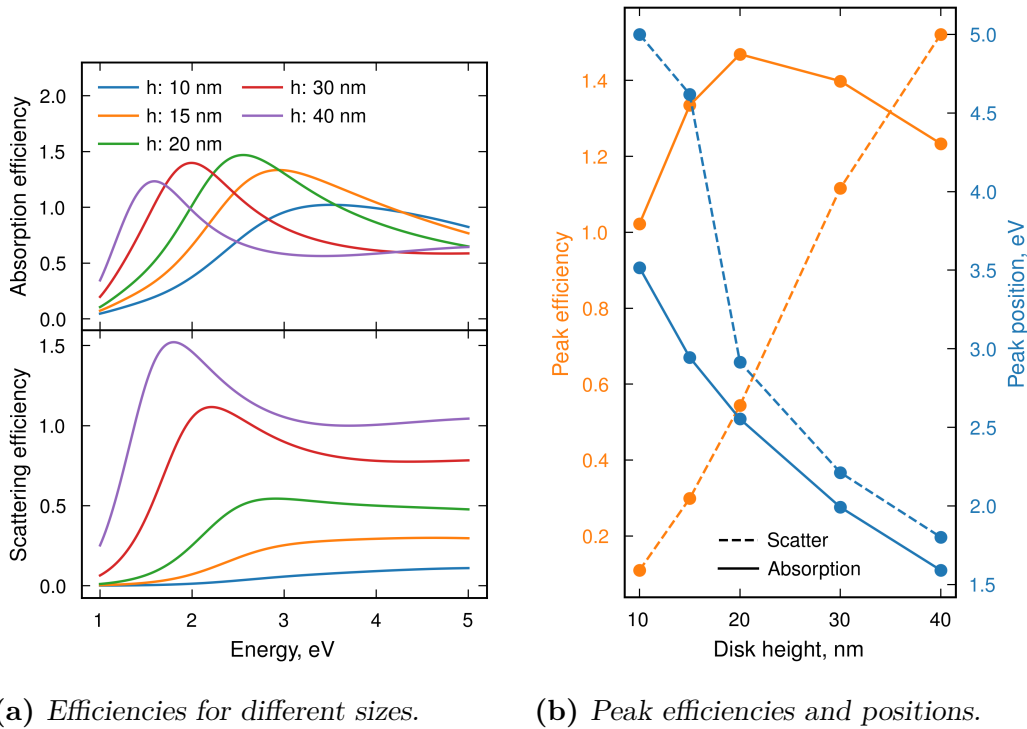


**Figure 6.6:** Variation of optical spectra with height and diameter of the truncated cone. Here the aspect ratio ( $AR$ ) is fixed at  $D/h = 5$  and the material is  $\text{Pd}_{0.83}\text{Au}_{0.17}$ . A clear red-shift in peak position can be seen with larger disk size. The peak scattering efficiency increases monotonically with size, while the absorption peak is maximal at a height of 20 nm.

## 6.4 Response due to lattice expansion

Since the size of the disk affects the optical spectra, as seen in the previous section, it is to be expected that additional strain, here due to the sorption of hydrogen, affects the optical spectra. The expansion due to hydrogenation can be modelled by simply scaling the length unit in MEEP, assuming the expansion to be isotropic. This effect is illustrated in Figure 6.7. Here, the optical spectra from nanodisks of  $\text{Pd}_{0.83}\text{Au}_{0.17}$  and  $\text{Pd}_{0.83}\text{Au}_{0.17}\text{H}_{0.67}$  are shown. The solid lines represent the physically sensible case where the lattice is allowed to expand, according to the data from Figure 3.2. Included is also a hypothetical case where the lattice is not allowed to expand, i.e. no size change is included, shown by the red dashed lines. The grey shaded area represents the change in the optical spectra due to the expansion of the lattice. It is small, but definitely noticeable, compared to the response due to change in dielectric properties. For comparison, the expansion was roughly 3% in each direction. From this point onward, the expansion due to hydrogen is included in all FDTD calculations.

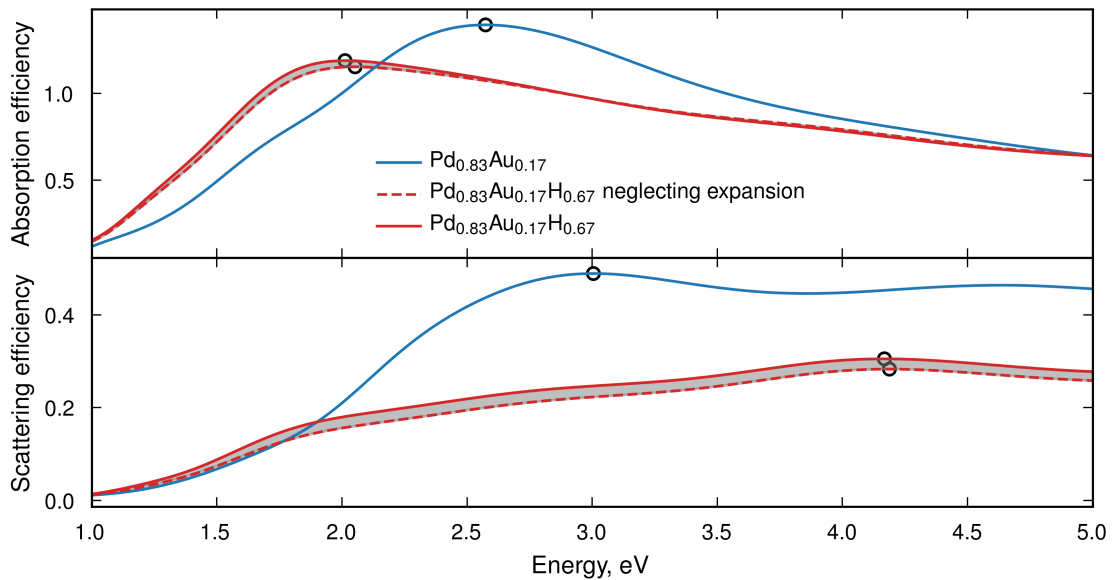


**Figure 6.7:** Impact of lattice expansion due to hydrogen on the optical spectra. The dashed lines correspond to the response where the expansion is neglected, i.e. a hypothetical non-physical case. The grey area is the change due to expansion. For reference the lattice parameter expansion was roughly 3%.

## 6.5 Total response due to hydrogenation

In this section the optical spectra of nanodisks with varying hydrogen and gold content will be presented. Some spectra will be shown and then the peak position will be studied further, since this is a descriptor that is most commonly measured experimentally.

In Figure 6.8 the extinction spectra for different gold and hydrogen concentrations of PdAu:H are shown. The truncated cone is 100 nm in diameter and 20 nm in height, with an angle of  $\theta = 60^\circ$ . For low hydrogen content the extinction peak is broad and centred at approximately 2.6 eV. Adding hydrogen shifts the peak to lower energies. This trend is true for all gold concentrations for this geometry and size. Higher gold content reduces the extinction efficiency for low hydrogen content, while additional hydrogen creates a sharp and intense extinction peak.

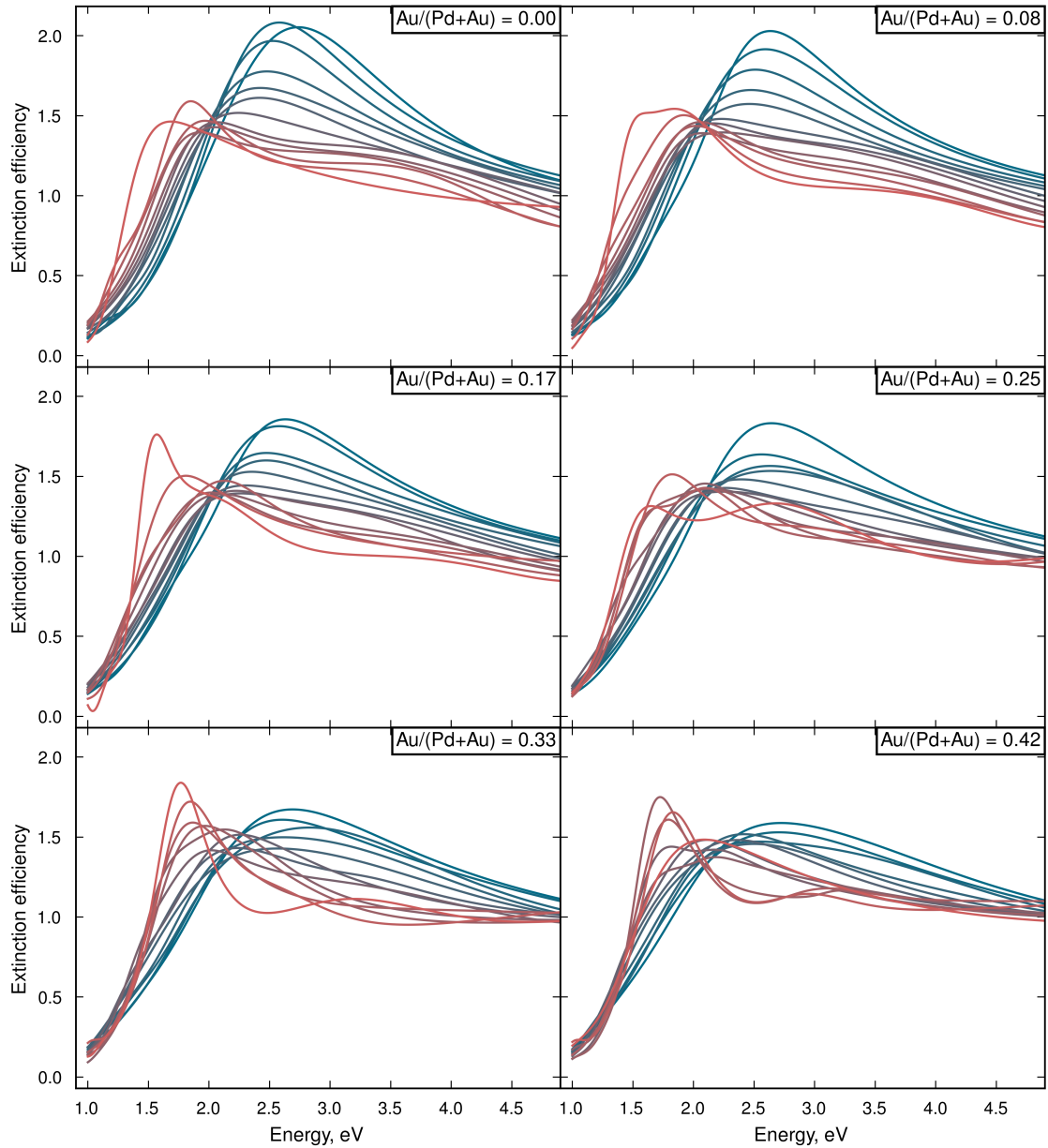


**Figure 6.8:** Spectra for the truncated cone geometry with diameter 100 nm and height 20 nm. The maximum number of oscillators allowed was 6. Redder lines correspond to higher hydrogen concentration. Here, only every second hydrogen concentration is plotted.

As an alternative representation, heat maps of the absorption spectra are shown for

two different gold concentrations in Figure 6.9. Here, the black domains are the peak positions for each hydrogen concentration. The red-shift of the peak position is clear and the two concentrations show, roughly, the same red-shift rate.

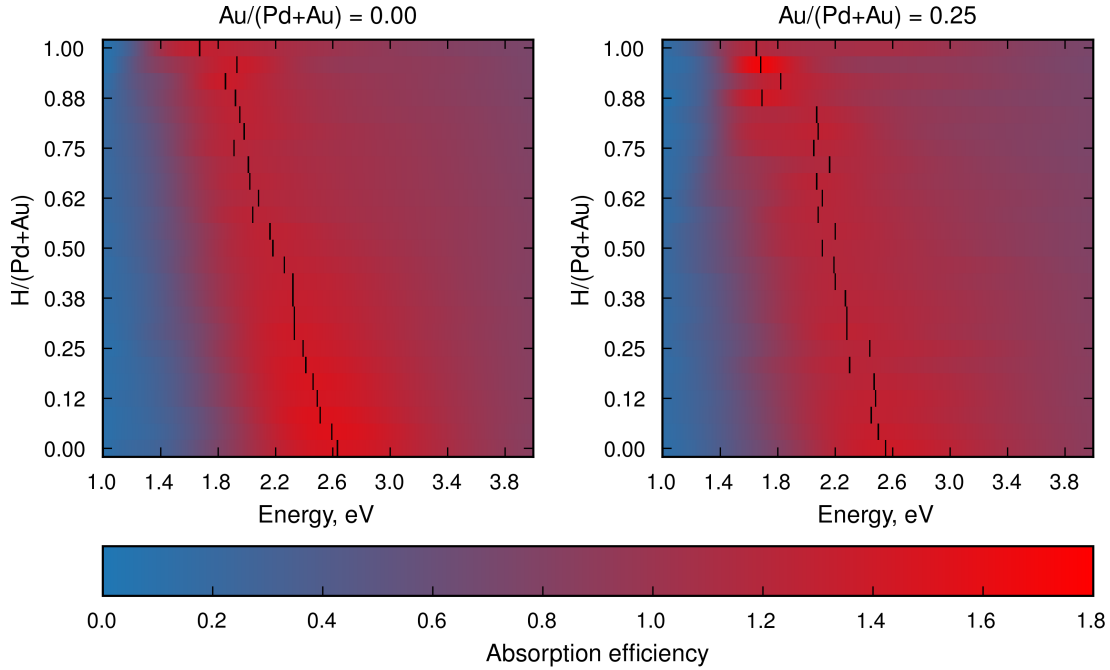
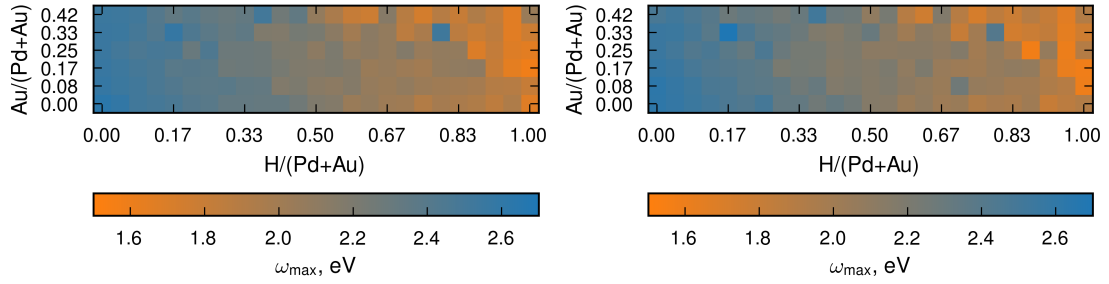


**Figure 6.9:** Heat map of the absorption efficiency for different hydrogen concentrations. The peak absorption energies are marked with black. The red-shift in peak position can be seen and the two gold concentrations show similar red-shift trends.

To further investigate the red-shift of the peak efficiency said quantity will now be studied furthered. In Figure 6.10 two heat maps of the peak absorption position is shown. The only difference between the two figures is the maximum number of oscillators in the Lorentzian fit. Qualitatively the trends are the same and overall the trends are quantitatively the same, except for a few outliers. Introducing hydrogen red-shifts the absorption peak from 2.6 eV to 1.6 eV.

In Figure 6.11 the absorption peak wavelength is presented as a function of hydrogen concentration. These data were obtained using the truncated cone geometry with a diameter of 100 nm, a height of 20 nm, and an angle of  $\theta = 60^\circ$ . A clear linear trend can be seen for most of the gold concentrations. At very high gold content larger deviations from the linear trend are observed. Experimentally a linear red-shift due to hydrogenation of PdAu-alloys has been measured for these types of geometries [34].



(a) Maximum 6 oscillators.

(b) Maximum 10 oscillators.

**Figure 6.10:** Heat map of peak absorption energy,  $\omega_{\max}$ , as a function of gold and hydrogen concentration. In the figure to the left/right the FDTD simulations were performed using a maximum of 6/10 oscillators. Both data sets show a red-shift due to hydrogenation and introduction of gold does affect this trend significantly.

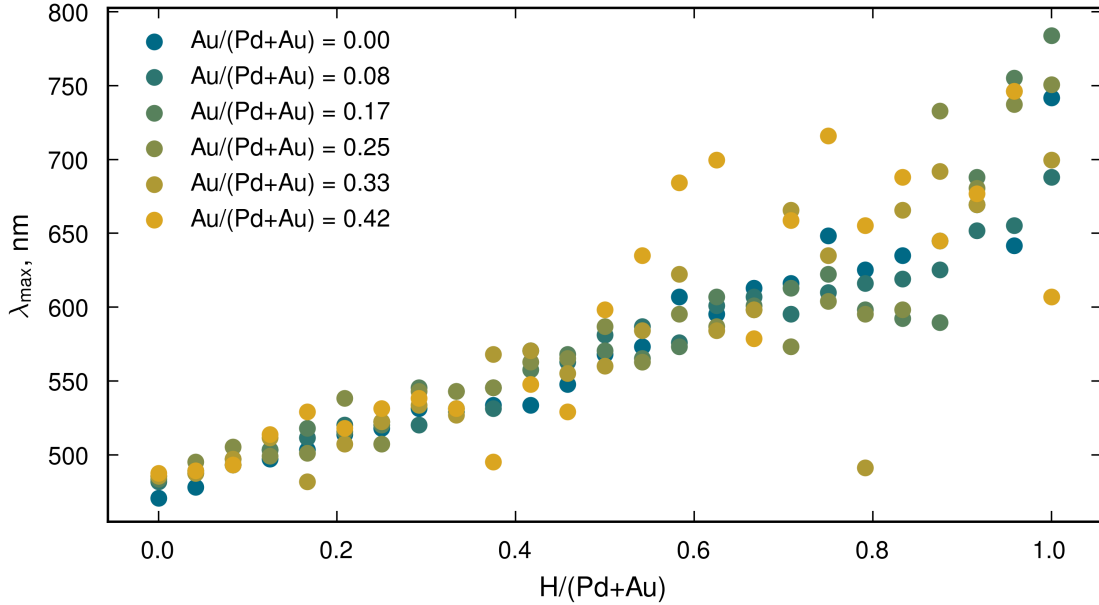


**Figure 6.11:** Absorption peak position as a function of hydrogen content. The red-shift is linear with respect to hydrogen concentration, for all of the sampled gold concentrations. Higher gold content lead to larger deviation from the linear trend.

## 6.6 Response of disks with different aspect ratios

The figures in the previous section showed an (approximately) linear trend in the red-shift due to hydrogenation. Interestingly this applies for all gold concentrations whereas the DFs in chapter 4 show much more variation than just a constant red-shift.

By changing the AR, where  $AR = D/h$ , of the sensor different energies of the DFs can be probed. In Figure 6.12 the AR is varied as the absorption peak position is

examined. A larger diameter results in a red-shift of the responses, which is expected. Interestingly at very small ARs the response is almost zero, if not negative. This suggests that altering the shape results in different slopes and thereby sensitivities. One can anticipate that it also is possible to drastically change the shape so that the response is outside of this energy interval, as a result of which new trends could emerge. Experimentally it has been observed that while the response is linear, the slope varies depending on the initial non-hydrogenated wavelength [34]. In other words, these results are in agreement with experimental results.

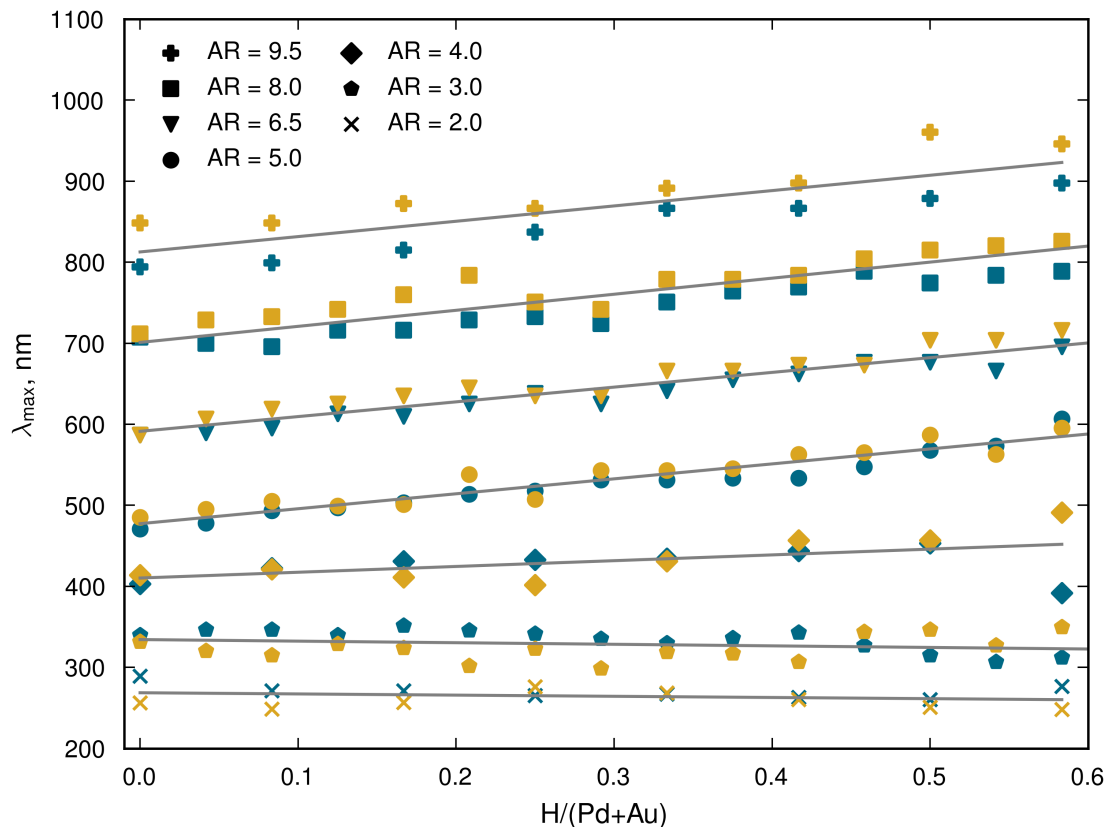


**Figure 6.12:** Here the absorption peak position is plotted against hydrogen concentration. This is done for two gold concentrations and for different ARs  $AR = D/h$  of the disk. The two alloys studied here were Pd and  $Pd_{0.75}Au_{0.25}$ . A clear red-shift can be seen for higher ARs, while the trend due to hydrogenation is the same, i.e. linear. Smaller ARs result in smaller responses and eventually the response might be a blue-shift due to hydrogenation.

To further investigate how sensitive the peak position is to hydrogen concentration for these types of Pd (and PdAu) disks the predicted sensitivities are presented and compared to experimental data. This is done in Figure 6.13. All of the values from this thesis are presented as the average of Pd and  $Pd_{0.75}Au_{0.25}$ . On the y-axis is essentially the slope from the previous figure and the x-axis is the peak position for the pure Pd (and PdAu) system. Two predicted values are included, one where the full hydrogen range is included and one which the range is limited. The experimental data is taken from a paper by Nugroho *et al.* [34] As a reminder:

the initial peak position is altered by changing the AR of the disks (this was also the case in the experimental study). Qualitatively the trends are similar. Initially a higher sensitivity is achieved by red-shifting the peak, but at some critical value there is no further gain in sensitivity. In the experimental paper the authors argue that this is not a plateau and that further red-shifting the initial peak will increase the sensitivity. This is motivated by looking at nanoparticles with a very different shape, which indeed lead to a red-shift in initial peak and a higher sensitivity (not presented here).

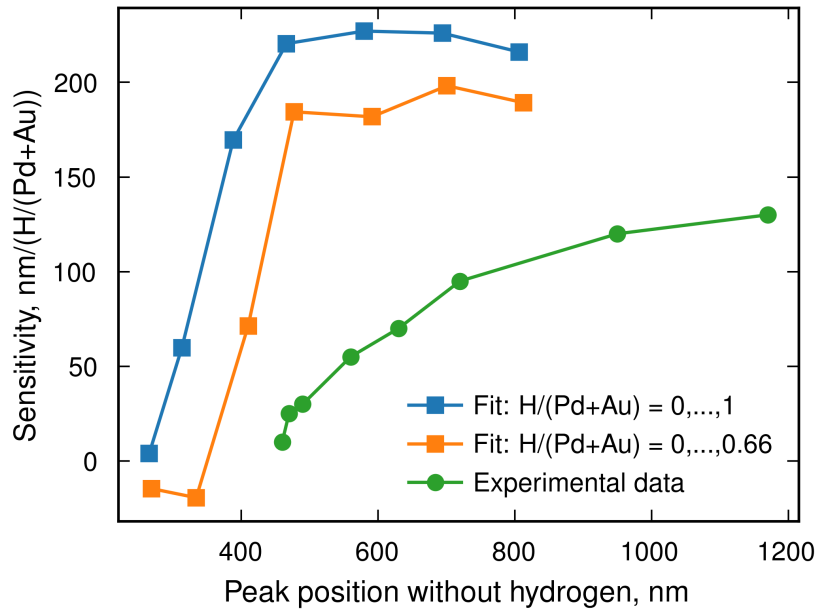


**Figure 6.13:** Calculated sensitivities from the FDTD simulations compared to experimental data. The experimental data is taken from Nugroho *et al.* The sensitivity is a measure of how much the peak shifts with hydrogen concentration, and it is the slope in Figure 6.12. Two fits are included, one where the slope is evaluated throughout the full concentration range and one with a smaller interval. Red-shifting the initial non-hydrogenated response leads to larger sensitivity initially but eventually the sensitivity seems to plateau.

## 6.7 Impact of microscopical configuration

In previous sections only the SQS versions of PdAu:H were studied. Here the optical spectra of SOSs and SQSs will be compared. In other words, the effect of microscopical configuration on the optical spectra will be investigated.

In Figure 6.14 the optical spectra of  $\text{Pd}_{0.83}\text{Au}_{0.17}$  and  $\text{Pd}_{0.83}\text{Au}_{0.17}\text{H}_{0.67}$  are shown. Here, the sensor is a truncated disk with diameter 100 nm and height 20 nm. Both the SQS and SOS versions of said materials are presented. There are small differences between the SQS and SOS cases. However, it should be noted that the unit cells of the SQSs and SOSs are of different sizes, containing 24 and 12 metal atoms

respectively. The difference is, probably, smaller than the accuracy of the Lorentzian fit and hence it is difficult to tell whether or not the microscopic ordering affects the optical properties.

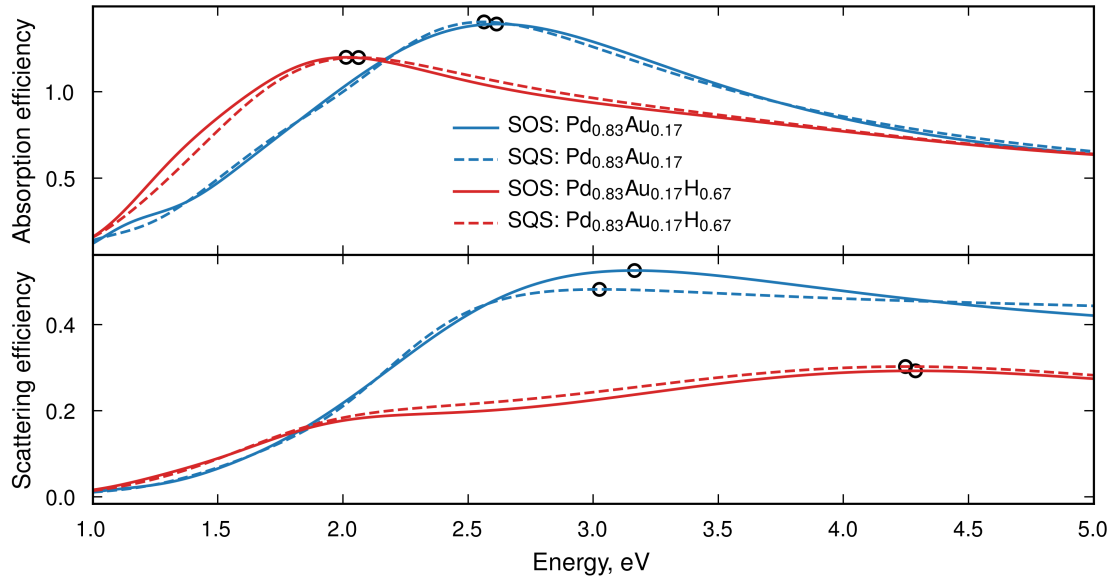


**Figure 6.14:** Optical spectra of SQS and SOS versions of  $Pd_{0.83}Au_{0.17}$  and  $Pd_{0.83}Au_{0.17}H_{0.67}$ . The differences are most likely smaller than the accuracy of the Lorentzian fitting.

To get a wider picture of the influence of microscopical ordering one can visualise the absorption peak position as a function of hydrogen content for the SQS and SOS cases. This is done in Figure 6.15. The shift in wavelength follows roughly the same trend. In this energy regime and for this shape and size of the sensor a distinct difference between the ordered and random case cannot be detected.

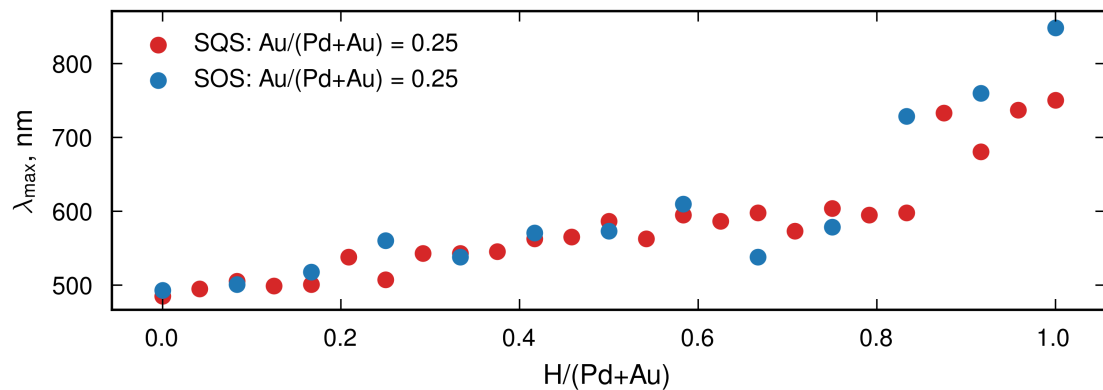


**Figure 6.15:** Red-shift of the absorption peak for ordered (SOS) and random (SQS) structures. Only one gold concentration is available, but for this case there is no detectable difference between thermodynamically representative and disordered structures.

## 6.8 Summary

The following list summarises the main results from the electromagnetic simulations:

- Truncated cones of PdAu with a diameter of 100 nm and height 20 nm show a linear red-shift in peak absorption wavelength as a function of hydrogenation. This was true for all studied gold concentrations. The response for this geometry was in the visible regime.
- It was shown that the lattice expansion due to hydrogenation is detectable in the optical spectra, but the change in the DF dominates the red-shift.
- Varying the AR results in a shift of the response. Furthermore a low AR result in essentially non-existing response due to hydrogenation. This was the case for sensors made of Pd and Pd<sub>0.75</sub>Au<sub>0.25</sub>.
- No significant difference between the optical response from SQSs and SOSs can be detected. In other words, the difference in the ordering of a random PdAu:H alloy and a thermodynamically representative structure of PdAu:H is not noticeable in the optical spectra, at least under the conditions considered here.



# 7

## Discussion and conclusion

The goal of thesis was to predict the optical response of PdAu:H alloys, and hence the capabilities of PdAu:H sensors from first-principles. This was successfully done for various sizes of truncated cones on the nanoscale. First the PdAu:H alloy itself was studied by combining CEs and MC simulations. Then smaller unit cells, were constructed from both the MC generated alloys and random alloys. The electronic properties of these special structures were calculated using static DFT and then the dielectric response was evaluated using TDDFT. Finally the optical response of nanodisks, with the dielectric properties described by the dielectric response calculated with TDDFT, were investigated. This was done with the electromagnetic simulation software MEEP. The software required the DFs to be expressed as a set of Lorentzians. Therefore, an efficient Lorentzian fitting method was developed.

The rest of this chapter summarises the main results from each chapter. Here some additional conclusions will be drawn by combining the results from different chapters, to explain some of the relations and connections between the chapters.

### 7.1 Ordering of PdAu:H alloy and its effect on spectra

In chapter 2 it was shown that in a randomised PdAu lattice introduced hydrogen atoms are more likely to be found near palladium than near gold in the nearest neighbour regime. In other words the nearest neighbour Pd-H bonds are more common than Au-H bonds. Interestingly if one examines second nearest neighbour pairs the opposite is true, i.e. Au-H and Pd-V pairs are the most common. The difference is clear when one studies the short range order parameter.

However, whether this affects the sensing capabilities of a PdAu nanodisk is not obvious. It was shown in chapter 4 and chapter 6 that the dielectric properties and optical spectra does not seem to be heavily affected. Here one should be careful since the SOSs and SQSs were differently sized, 12 and 24 atoms respectively, which could play a role in how representative the final dielectric functions in the two cases are. It is also worthwhile mentioning that *if* there is a small difference in the dielectric function, the Lorentzian fitting might not capture it. It is likely that the difference is in fact negligible, which would allow future research of optical properties for PdAu:H to neglect the ordering and simply assume that the alloy is a random alloy.

## 7.2 Electronic structure and dielectric response for PdAu:H

The electronic properties of PdAu:H alloys were investigated in chapter 3. There it was shown, by studying the band structure and DOS, that hydrogenation of PdAu pushes down the band in vicinity to the Fermi level and eventually the whole band is occupied. Introducing more gold in the PdAu alloy results in the same phenomena. For reference gold has a totally filled d-band circa 2 eV below the Fermi level and palladium has a band intercepting the Fermi level. This can be interpreted in the following way: introducing hydrogen in palladium generates more gold-like properties in the palladium. Interestingly, this is also true for PdAu alloys, at least when the gold concentrations below circa 42 %.

This seems to be true also for the DF of PdAu:H. In the visible limit the loss function,  $-\text{Im}\{1/\epsilon\}$ , behaves similarly for the various gold concentrations. The details in the function is red-shifted in a monotonous fashion when hydrogen is added. Typically gold shows a peak in the imaginary part of the dielectric function at circa 2 eV due to interband transitions. This is similar to the broad feature in loss function for PdAu:H at circa 3 eV. Hence the interpretation that Pd:H shows resemblance to gold is somewhat reasonable when looking at the dielectric properties.

## 7.3 Optical response due to hydrogenation

In the end it is the change in optical spectra and the shift in the extinction peak due to hydrogenation that determines how well a plasmonic sensor functions. This was studied in chapter 6. In summary, truncated cones of PdAu with diameter 100 nm and height 20 nm showed a linear red-shift in peak position due to hydrogenation. The slope was approximately  $\Delta\lambda_{\text{max}}/\Delta c_H = 200 \text{ nm}$ , where  $\Delta c_H = \text{H}/(\text{Pd} + \text{Au})$ . This relation was found for all gold concentrations, although at higher gold and hydrogen concentrations the peak positions fluctuated more.

However, changing the aspect ratio  $\text{AR} = D/h$  of the disk results in a change in the magnitude of the response and in the initial peak position. In other words changing the AR results in different sensitivity of the device. It should be noted that the response was typically linear, but non-linearities could emerge for certain shapes. It was found that the sensitivity increased with a larger AR, but eventually the sensitivity plateaued. This is in agreement with experimental work done by Nugroho *et al.* In their work the sensitivity increased with AR until a plateau was hit. In the article they claim that this is not a plateau, with the motivation that for nanorings the sensitivity further increased. However, this was not investigated in this thesis.

In general the extinction peak for PdAu:H disks with  $\text{AR} = 5$  and low hydrogen content were typically broader and centred around 2.6 eV. A higher hydrogen content red-shift the peaks, as explained above, but additionally the width of the peaks get smaller for more hydrogen rich structures. This property could be used in sensing applications. The decrease in the width is likely due to the decrease in the imaginary part of the DF with hydrogen, since this results in a sharper peak.

# Bibliography

- [1] T. Hübert, L. Boon-Brett, G. Black, and U. Banach. Hydrogen sensors – A review. *Sensors and Actuators B: Chemical*, 157(2):329–352, October 2011.
- [2] Brian D. Adams and Aicheng Chen. The role of palladium in a hydrogen economy. *Materials Today*, 14(6):282–289, June 2011.
- [3] F. D. Manchester, A. San-Martin, and J. M. Pitre. The H-Pd (hydrogen-palladium) System. *Journal of Phase Equilibria*, 15(1):62–83, February 1994.
- [4] R. Burch and R. G. Buss. Absorption of hydrogen by palladium–copper alloys. Part 1.—Experimental measurements. *Journal of the Chemical Society, Faraday Transactions 1: Physical Chemistry in Condensed Phases*, 71(0):913, 1975.
- [5] Z. Zhao, Y. Sevryugina, M. A. Carpenter, D. Welch, and H. Xia. All-Optical Hydrogen-Sensing Materials Based on Tailored Palladium Alloy Thin Films. *Analytical Chemistry*, 76(21):6321–6326, November 2004.
- [6] Kathryn M. Mayer and Jason H. Hafner. Localized Surface Plasmon Resonance Sensors. *Chemical Reviews*, 111(6):3828–3857, June 2011.
- [7] Carl Wadell, Ferry Anggoro Ardy Nugroho, Emil Lidström, Beniamino Iandolo, Jakob B. Wagner, and Christoph Langhammer. Hysteresis-Free Nanoplasmonic Pd–Au Alloy Hydrogen Sensors. *Nano Letters*, 15(5):3563–3570, May 2015.
- [8] Mattias Ångqvist, William A. Muñoz, J. Magnus Rahm, Erik Fransson, Céline Durniak, Piotr Rozyczko, Thomas H. Rod, and Paul Erhart. ICET – A Python library for constructing and sampling alloy cluster expansions. *Advanced Theory and Simulations*, 2(7):1900015, 2019.
- [9] Alex Zunger, S.-H. Wei, L. G. Ferreira, and James E. Bernard. Special quasirandom structures. *Physical Review Letters*, 65(3):353–356, July 1990.
- [10] A. van de Walle, P. Tiwary, M. de Jong, D.L. Olmsted, M. Asta, A. Dick, D. Shin, Y. Wang, L.-Q. Chen, and Z.-K. Liu. Efficient stochastic generation of special quasirandom structures. *Calphad*, 42:13–18, 2013.
- [11] Magnus Rahm, 2020. private communication.
- [12] Jürgen Hafner. *Ab-Initio* simulations of materials using VASP: Density-functional theory and beyond. *Journal of Computational Chemistry*, 29(13):2044–2078, 2008.
- [13] J. J. Mortensen, L. B. Hansen, and K. W. Jacobsen. Real-space grid implementation of the projector augmented wave method. *Physical Review B*, 71(3):035109, 2005.
- [14] J Enkovaara, C Rostgaard, J J Mortensen, J Chen, M Dułak, L Ferrighi, J Gavnholt, C Glinsvad, V Haikola, H A Hansen, H H Kristoffersen, M Kuusma, A H Larsen, L Lehtovaara, M Ljungberg, O Lopez-Acevedo, P G Moses, J Oja-

- nen, T Olsen, V Petzold, N A Romero, J Stausholm-Møller, M Strange, G A Tritsarlis, M Vanin, M Walter, B Hammer, H Häkkinen, G K H Madsen, R M Nieminen, J K Nørskov, M Puska, T T Rantala, J Schiøtz, K S Thygesen, and K W Jacobsen. Electronic structure calculations with GPAW: A real-space implementation of the projector augmented-wave method. *Journal of Physics: Condensed Matter*, 22(25):253202, 2010.
- [15] Jun Yan, Jens. J. Mortensen, Karsten W. Jacobsen, and Kristian S. Thygesen. Linear density response function in the projector augmented wave method: Applications to solids, surfaces, and interfaces. *Physical Review B*, 83(24):245122, 2011.
- [16] Richard M Martin. *Electronic Structure: Basic Theory and Practical Methods*. Cambridge University Press, 2012.
- [17] M. Dion, H. Rydberg, E. Schröder, D. C. Langreth, and B. I. Lundqvist. Van der waals density functional for general geometries. *Physical Review Letters*, 92(24):246401, June 2004.
- [18] Kristian Berland and Per Hyldgaard. Exchange functional that tests the robustness of the plasmon description of the van der Waals density functional. *Physical Review B*, 89(3):035412, 2014.
- [19] Leili Gharaee, Paul Erhart, and Per Hyldgaard. Finite-temperature properties of nonmagnetic transition metals: Comparison of the performance of constraint-based semilocal and nonlocal functionals. *Physical Review B*, 95(8):085147, 2017.
- [20] Georg Alefeld. *Hydrogen in Metals. 1: Basic Properties*. Number 28 in Topics in Applied Physics. Springer, Berlin, 1978. OCLC: 60428388.
- [21] M. Kuisma, J. Ojanen, J. Enkovaara, and T. T. Rantala. Kohn-Sham potential with discontinuity for band gap materials. *Physical Review B*, 82(11):115106, 2010.
- [22] Miguel A.L. Marques, Neepa T. Maitra, Fernando M.S. Nogueira, E.K.U. Gross, and Angel Rubio, editors. *Fundamentals of Time-Dependent Density Functional Theory*, volume 837 of *Lecture Notes in Physics*. Springer Berlin Heidelberg, Berlin, Heidelberg, 2012.
- [23] Stephen L. Adler. Quantum Theory of the Dielectric Constant in Real Solids. *Physical Review*, 126(2):413–420, April 1962.
- [24] Nathan Wisser. Dielectric Constant with Local Field Effects Included. *Physical Review*, 129(1):62–69, January 1963.
- [25] Carsten A. Ullrich. *Time-Dependent Density-Functional Theory : Concepts and Applications*. Oxford University Press, 2012.
- [26] Carsten A. Ullrich and Zeng-hui Yang. A Brief Compendium of Time-Dependent Density Functional Theory. *Brazilian Journal of Physics*, 44(1):154–188, 2014.
- [27] Ardavan F. Oskooi, David Roundy, Mihai Ibanescu, Peter Bermel, J.D. Joannopoulos, and Steven G. Johnson. Meep: A flexible free-software package for electromagnetic simulations by the FDTD method. *Computer Physics Communications*, 181(3):687–702, 2010.

- [28] Ron Rubinstein, Michael Zibulevsky, and Michael Elad. Efficient Implementation of the K-SVD Algorithm using Batch Orthogonal Matching Pursuit. *CS Technion*, 2008.
- [29] Fredrik Eriksson, Erik Fransson, and Paul Erhart. The hiphive package for the extraction of high-order force constants by machine learning. *Advanced Theory and Simulations*, 2:1800184, 2 2019.
- [30] Kenneth P. Burnham and David R. Anderson. Multimodel Inference: Understanding AIC and BIC in Model Selection. *Sociological Methods & Research*, 33(2):261–304, 2004.
- [31] Robert L. Olmon, Brian Slovick, Timothy W. Johnson, David Shelton, Sang-Hyun Oh, Glenn D. Boreman, and Markus B. Raschke. Optical dielectric function of gold. *Physical Review B*, 86(23):235147, 2012.
- [32] Aleksandar D. Rakić, Aleksandra B. Djurišić, Jovan M. Elazar, and Marian L. Majewski. Optical properties of metallic films for vertical-cavity optoelectronic devices. *Applied Optics*, 37(22):5271, 1998.
- [33] Allen Taflove, Ardavan Oskooi, and Steven G Johnson. *Advances in FDTD Computational Electrodynamics: Photonics and Nanotechnology*. Artech House, 2013.
- [34] Ferry Anggoro Ardy Nugroho, Iwan Darmadi, Vladimir P. Zhdanov, and Christoph Langhammer. Universal Scaling and Design Rules of Hydrogen-Induced Optical Properties in Pd and Pd-Alloy Nanoparticles. *ACS Nano*, 12(10):9903–9912, 2018.

